

This is a non-peer-reviewed preprint submitted to EarthArXiv.

This manuscript has been submitted for publication. Please note the manuscript has yet to be formally accepted for publication. Subsequent versions of this manuscript may have slightly different content. If accepted, the final version of this manuscript will be available via the 'Peer-reviewed Publication DOI' link on the right-hand side of this webpage. Please feel free to contact any of the authors; we welcome feedback.

# Biomineralization for Sustainable Ecotoxic Metal Immobilisation via Enzyme Induced Carbonate Precipitation

Dickinson, Heloisa<sup>a</sup>; MacDonald, John<sup>a</sup>; Toney, Jaime L.<sup>a</sup> <sup>a</sup>School of Geographical and Earth Sciences, University of Glasgow

#### Abstract

Heavy metal contamination of water presents a critical global challenge driven by the persistence and toxicity of elements such as arsenic, cadmium and lead. Conventional remediation strategies, such as Enzyme-Induced Carbonate Precipitation (EICP), typically rely on commercial urease and a multi-step extraction process, which increases energy demand, generates ammonium byproducts, and requires significant chemical inputs. In this study, we introduce a streamlined EICP approach employing crude soybean urease extract to treat a wide range of nine ecotoxic metals (As, Cd, Co, Cr, Cu, Li, Ni, Pb, Zn) in aqueous solutions. Crystallographic and morphological analyses revealed calcite as a recurring phase across all treatments, with element-specific carbonate minerals, such as otavite (cadmium carbonate) and cerussite (lead carbonate), detected in the corresponding systems. The method integrates low-power juicing, single-step filtration, and minimal reagent use, delivering effective removal, while only arsenic and copper exhibited notable enzymatic inhibition. The adaptive workflow achieved a 54.4% reduction in total CO2e emissions compared with conventional extraction protocols. Compared with conventional protocols, the proposed adaptive optimisation workflow lowered energy demand, reduced chemical inputs, and mitigated greenhouse gas emissions. By incorporating waste-derived calcium and urea, the process establishes a closed-loop cycle, offering pathways for application in engineered treatment plants, active dosing systems, or passive remediation schemes. Future work should focus on mixed-metal systems and molecular-scale mechanisms to strengthen the foundation for the field-scale deployment of this sustainable strategy.

#### 1. Introduction

Ecotoxic metal (EM) contamination in soil and water is among the most critical environmental challenges of the 21<sup>st</sup> century (UNEP, 2021). Anthropogenic activities such as industrial processes, vehicle emissions, and agricultural runoff have led to the widespread release of ecotoxic metals into terrestrial and aquatic environments. Due to their non-biodegradable nature, these contaminants persist for decades in soils and water bodies, posing environmental and public health risks, including ecosystem degradation, biodiversity loss, and human exposure through direct contact, ingestion, or contaminated food and water. In urban areas, where most of the global population is concentrated and continues to grow, climate change and the urban heat island effect combine with existing pollution to intensify thermal stress, alter hydrological cycles, and

increase the mobility and bioavailability of contaminants [Wu et al., 2024, Shi et al., 2012].

Given the widespread and persistent nature of urban pollution, various soil and water remediation strategies have been developed in recent decades, including chemical, physical, and biological methods. However, many conventional approaches face challenges related to cost, scalability, or environmental compatibility. As a result, biomineralization-based techniques have gained attention for their ability to generate stable mineral phases that immobilise ecotoxic metals. One such method, enzyme-induced carbonate precipitation (EICP), employs urease extracted from non-microbial sources, typically plants like soybean and sword bean. By catalysing urea hydrolysis, urease produces ammonia and carbonate ions that drive calcium carbonate formation, offering a biosafe and controllable alternative to microbially induced carbonate precipitation (MICP) (Saif et al., 2022; Rajasekar et al., 2025; Bian et al., 2024). A concurrent by-product of the MICP reaction is ammonium (NH<sub>4</sub><sup>+</sup>), which may pose environmental concerns if not managed appropriately, representing an important consideration for large-scale implementation (Saif et al., 2022; Rajasekar, 2025).

The alkalinity generated during EICP reactions further enhances carbonate ion concentrations, favouring CaCO<sub>3</sub> precipitation while simultaneously lowering metal solubility. Metals may then be immobilised through discrete carbonate phases (e.g., cerussite, smithsonite) (Li et al, 2022; Wang et al., 2022), solid-solution substitution within calcite/aragonite lattices (Wang et al., 2023; Zeng et al., 2025), or by coprecipitation and adsorption processes (Bian et al., 2024; Wang et al., 2023).

Biomolecules present in crude urease extracts, such as proteins, amino acids, and polysaccharides, have been shown to modulate mineral nucleation, influence crystal morphology, and enhance the stability of both crystalline and amorphous metalbearing phases (Chen et al., 2024, 2025; Orme et al., 2001; Sikiric et al., 2006). These crude soybean urease extracts contain amino acids, proteins, and polysaccharides that expose functional groups (e.g., carboxyl, amine, and phenolic). These organic molecules can bind Ca<sup>2+</sup> ions, act as heterogeneous nucleation sites, and adsorb onto crystal planes, thereby influencing the morphology, growth, and distribution of CaCO<sub>3</sub> during EICP (Shu et al., 2022; Chen et al., 2025).

Several studies have demonstrated the potential of enzyme-induced carbonate precipitation (EICP) for aqueous-phase ecotoxic metal remediation. These works have focused on different aspects of the technique, ranging from optimising calcium sources and urease activity to elucidating crystallisation pathways and assessing long-term stability in selected metal systems. Abdel-Gawwad et al. (2020) showed efficient removal of  $Pb^{2+}$ ,  $Cu^{2+}$  and  $Ni^{2+}$ , with lead almost completely immobilised as nano-carbonates within hours. Wang et al. (2022) examined how urease concentration and calcium source influence  $Pb^{2+}$  removal, reporting near-complete immobilisation and proposing a precipitation sequence from  $PbCl_2$  to  $PbCO_3$  and  $CaCO_3$ . Li et al. (2022) focused on  $Cd^{2+}$ , demonstrating concurrent mechanisms of nucleation, chemisorption and coprecipitation, with crystalline otavite identified as the dominant product in systems with carbonate precipitation of  $Mg^{2+}/Ca^{2+}$ . Bian et al. (2024) highlighted that moderate  $Ca^{2+}$ 

concentrations enhanced the immobilisation of Zn<sup>2+</sup> and Ni<sup>2+</sup>, whereas excess Ca<sup>2+</sup> suppressed urease activity, and further noted that organic molecules may stabilise poorly crystalline carbonate phases. Most recently, Zeng et al. (2025) utilised soybean-derived urease to generate porous vaterite capable of selectively adsorbing Cu<sup>2+</sup>, Pb<sup>2+</sup> and Cd<sup>2+</sup>, achieving exceptionally high sorption capacities and maintaining over 80% efficiency for Cd<sup>2+</sup> after several weeks. Collectively, these findings demonstrate that metal retention via EICP is predominantly governed by pH, calcium availability and species, and the biochemical composition of the urease extracts. To provide a consolidated overview of the recent progress in this area, Table 1 summarises the key conditions and outcomes reported in studies employing EICP for the removal of ecotoxic metals from aqueous solutions. The table highlights differences in target metals, reagent concentrations, urease sources and activities, removal efficiencies, and the mineral phases identified. This synthesis underscores both the versatility of EICP and the variability of outcomes depending on system-specific factors.

The mineralogical properties of carbonate phases formed during EICP play a key role in determining both the long-term stability of immobilised metals and the potential for carbon storage. Calcite, the thermodynamically stable polymorph of calcium carbonate, is more resistant to dissolution and transformation than metastable forms such as vaterite or amorphous carbonates (Morse et al., 2007). Its formation not only supports durable metal retention (Chen et al., 2024) but also enables the incorporation of atmospheric or waste-derived  $CO_2$ , providing dual environmental benefits (Bian et al., 2025; Zhao et al., 2024; Hemayati et al., 2024).

This is the first study to systematically assess EICP performance across a wide range of ecotoxic metals under controlled aqueous conditions. In addition, we propose the concept of adaptive optimisation, a feedback-driven strategy that streamlines crude urease workflows, reduces chemical inputs, and aligns with circular economy principles. Together, these contributions lay the groundwork for scalable and sustainable deployment of EICP-based remediation strategies. In this paper, we evaluated the performance of EICP in immobilising As, Cd, Co, Cr, Cu, Li, Ni, Pb, and Zn, at concentrations of 2, 5, and 20 millimolar in aqueous systems. Four key parameters were assessed: final pH, precipitate mass, ammonium production, and metal removal efficiency. In addition, mineralogical characterisation of the solid products was conducted using scanning electron microscopy and X-ray diffraction with Rietveld refinement to identify and quantify the crystalline phases.

Table 1. Summary of recent studies employing or revising EICP for the removal of ecotoxic metals from aqueous solutions. Conditions include metal concentration, urea and calcium chloride dosages, urease source and activity, removal efficiency, and mineral phases identified via XRD or other characterisation methods. Urease activity is reported either as enzymatic units (U/g or U/mL) or as urea hydrolysis rate (mM urea min<sup>-1</sup>) depending on the method used (EC: electrical conductivity; Nessler's; indophenol blue).

Study	Metal(s)	Metal conc.	Urea (M)	CaCl₂ (M)	Urease source	Urease activity	Removal Efficiency	Phases Identified
Xu et al. (2025)	Cd <sup>2+</sup> , Pb <sup>2+</sup> , Cu <sup>2+</sup>	1.5–1.7 mM (per metal; mg L <sup>-1</sup> varies by metal)	0.25–1.0	0.25–1.0	Defatted soybean meal, cold extract, crude	0.5–2.0 U/mL (indophenol blue method)	Cd <sup>2+</sup> : 98.7% Pb <sup>2+</sup> : 99.1% Cu <sup>2+</sup> : 95.3%	Cerussite (PbCO <sub>3</sub> ) Otavite (CdCO <sub>3</sub> ) Malachite (Cu <sub>2</sub> (OH) <sub>2</sub> CO <sub>3</sub> ) Amorphous CaCO <sub>3</sub> observed in all treatments
Zeng et al. (2025)*	Cd <sup>2+</sup> , Pb <sup>2+</sup> , Cu <sup>2+</sup>	200 mg L <sup>-1</sup> (single- metal); 100 mg L <sup>-1</sup> each (multi-metal)	0.2–1.6 (1:1 with Ca <sup>2+</sup> ; 0.8 optimum for vaterite synthesis)	0.2–1.6 (0.8 optimum)	Soybean- derived crude urease	18 U (diluted to 9 U for synthesis), Nessler method	Individual systems: $^{\circ}$ 88–97% removal within days; Langmuir $q_m$ : $Cu^{2+}$ 1207 mg $g^{-1} > Cd^{2+}$ 786 mg $g^{-1} > Pb^{2+}$ 655 mg $g^{-1}$ ; multi-metal shows competition	Sorbent: vaterite (CaCO <sub>3</sub> ) → partial calcite over time; Products: CdCO <sub>3</sub> , PbCO <sub>3</sub> / Pb <sub>3</sub> (CO <sub>3</sub> ) <sub>2</sub> (OH) <sub>2</sub> ; Cu <sup>2+</sup> : Cu <sub>2</sub> Cl(OH) <sub>3</sub> (in Cl <sup>-</sup> media)
Chen et al. (2024)	Zn <sup>2+</sup>	10mM	0.5	0.5	Canavalia ensiformis (jack bean) and C. gladiata (sword bean)	1.0 g/L crude extract (no mention of urease activity)	Zn <sup>2+</sup> : 98.1–99.4%	$ZnCO_3$ , $Zn(OH)_2$ , $Zn_5(CO_3)_2(OH)_6$
Bian et al. (2024)	Zn <sup>2+</sup> , Ni <sup>2+</sup>	≈3.06 mM Zn <sup>2+</sup> ≈3.41 mM Ni <sup>2+</sup>	0.75	0, 0.25, 0.5	Canavalia gladiata (sword bean), crude extract	~15 mM urea min <sup>-1</sup> (ammonium-rate method, at 25 g L <sup>-1</sup> extract)	Zn <sup>2+</sup> : 98.7% Ni <sup>2+</sup> : 62.4%	$ZnCO_3$ , $Zn(OH)_2$ , $Zn_5(CO_3)_2(OH)_6$ , $NiCO_3$
Wang et al. (2023)	Pb <sup>2+</sup> , Cu <sup>2+</sup>	5–50mM	0.5	0.25	Canavalia ensiformis (jack bean) crude, ethanol- extracted	342.7 U⋅g <sup>-1</sup> (Nessler); ≈5.06 mM urea⋅min <sup>-1</sup> (Whiffin method)	≈100% across 5–50 mM	Biotic: cerussite PbCO <sub>3</sub> , phosgenite Pb <sub>2</sub> Cl <sub>2</sub> CO <sub>3</sub> (when CO <sub>3</sub> <sup>2-</sup> limited); Abiotic: cotunnite PbCl <sub>2</sub> , Pb(OH)Cl
Li et al. (2022)	Cd <sup>2+</sup>	5.46 mM	0.333	Ca/Mg supplied as acetates; five Mg:Ca sets (mM:mM):	Canavalia ensiformis (jack bean)	5 U/mL Nessler's colour reagent (NCR) assay	≥99.9% Cd	Otavite $(CdCO_3)$ ; calcite $(CaCO_3)$ with $Cd$ coprecipitation; vaterite/aragonite $(CaMg(CO_3)_2)$ with

				10:10, 20:10, 30:10, 20:20, 20:6.7				chemisorption; dolomite present
Wang et al. (2022a)	Pb <sup>2+</sup> , Cu <sup>2+</sup>	5, 10, 30, 40, 50 mM	0.5	0.25 (CaCl <sub>2</sub> , Ca(CH <sub>3</sub> COO) <sub>2</sub> , CaO)	Canavalia ensiformis (jack bean) crude, ethanol- extracted	342.7 U·g <sup>-1</sup> (Nessler)	Pb <sup>2+</sup> : up to ~99% (CaCl <sub>2</sub> best), Cu <sup>2+</sup> : up to ~95% (CaO best); strong dependence on pH and hydrolysis suppression	CaCl <sub>2</sub> : cerussite, hydrocerussite, phosgenite, Pb(OH)Cl, PbCl <sub>2</sub> ; Ca(CH <sub>3</sub> COO) <sub>2</sub> : cerussite, hydrocerussite, Pb(OH) <sub>2</sub> ; CaO: Pb(OH) <sub>2</sub> dominant; Cu phases: malachite, azurite, atacamite (CaCl <sub>2</sub> ), CuO (CaO, Ca- acetate)
Wang et al. (2022b)	Pb <sup>2+</sup>	5, 10, 30, 40, 50 mM	0.5	0.25	Canavalia ensiformis (jack bean), crude extract	342.7 U/g (Nessler's reagent colorimetric) or 99.8 mM urea min <sup>-1</sup> (EC)	> 99.5% for all treatments	Biotic: cerussite PbCO <sub>3</sub> , hydrocerussite Pb <sub>3</sub> (CO <sub>3</sub> ) <sub>2</sub> (OH) <sub>2</sub> , calcium carbonate CaCO <sub>3</sub> Abiotic: cotunnite PbCl <sub>2</sub> , lead hydroxide Pb(OH) <sub>2</sub> , calcium hydroxide Ca(OH) <sub>2</sub>
Li et al. (2022)	Cd <sup>2+</sup>	5.46 mM	0.333	Ca/Mg supplied as acetates; five Mg:Ca sets (mM:mM): 10:10, 20:10, 30:10, 20:20, 20:6.7	Canavalia ensiformis (jack bean)	5 U/mL Nessler's colour reagent (NCR) assay	≥99.9% Cd	Otavite (CdCO <sub>3</sub> ); calcite (CaCO <sub>3</sub> ) with Cd coprecipitation; vaterite/aragonite (CaMg(CO <sub>3</sub> ) <sub>2</sub> ) with chemisorption; dolomite present
Abdel- Gawwad et al. (2020)	Pb <sup>2+</sup> , Cu <sup>2+</sup> , Ni <sup>2+</sup>	50–200 mM	0.05–0.20	No source of Ca	Canavalia ensiformis (jack bean) crude	1 mg of PDUE hydrolyses ~3 mg of urea	Pb ≈99–100% Cu ≈67–68%; Ni ≈58%	Cerussite (PbCO $_3$ , 4–15 nm); malachite hexahydrate (CuCO $_3$ ·Cu(OH) $_2$ ·6H $_2$ O, ~8 nm—thick sheets); hellyerite (NiCO $_3$ ·6H $_2$ O, ~0.30 $\mu$ m—thick sheets)
Rajasekar et al. (2025)	Rajasekar et al. (2025) conducted a non-experimental comparative review of MICP and EICP for heavy-metal remediation, synthesising mechanisms, operational conditions (pH/temperature/urease sources), reported efficiencies and typical carbonate phases, and discussing the advantages and limitations of each approach.							

<sup>\*</sup> EICP used to synthesize vaterite; metal removal assessed by adsorption with pre-formed CaCO<sub>3</sub>, not in situ EICP precipitation.

#### 1.1. Theoretical Framework: EICP and Ecotoxic Metal Immobilization

Enzyme-Induced Carbonate Precipitation (EICP) is a bio-mediated strategy for the immobilisation of heavy metals in contaminated matrices. It relies on the urease-catalysed hydrolysis of urea, generating ammonium and carbonate ions according to the reaction (Gilmour et al., 2024):Nemati & Voordouw, 2003):

$$CO(NH_2)_2 + H_2O \xrightarrow{urease} 2NH_3 + CO_2$$
 (Equation 1)

This is followed by the conversion of  $CO_2$  in water to carbonate ions under alkaline conditions. The overall process increases pH and promotes supersaturation with respect to calcium carbonate, enabling mineral precipitation (Ahenkorah et al., 2021):

$$Ca^{2+} + CO_3^{2-} \rightarrow CaCO_3 \downarrow$$
 (Equation 2)

These precipitates function both as structural scaffolds and as active phases that sequester metal ions through inorganic and organic pathways. Inorganic immobilisation involves multiple mineralogical mechanisms: co-precipitation with CaCO<sub>3</sub> via surface adsorption, isomorphic substitution (e.g. Cd<sup>2+</sup>, Zn<sup>2+</sup> partially replacing Ca<sup>2+</sup> in the calcite lattice forming solid solutions), occlusion within growing crystals, or mechanical entrapment among crystal aggregates (Kim et al., 2023; Xu et al., 2025). These substitution processes can be expressed by the general solid-solution reaction:

$$CaCO_3(s) + x M^{2+} \rightleftharpoons Ca_{1-x}M_xCO_3(s) + x Ca^{2+}$$
 (solid solution) (Equation 3)

In the context of EICP, thermodynamic modelling and experimental studies confirm that metals such as  $Ni^{2+}$ ,  $Cd^{2+}$ , and  $Pb^{2+}$  can be incorporated into calcite lattices through surface and subsurface substitution (Xu et al., 2025). When the solubility product of a given metal carbonate is sufficiently low, discrete phases such as cerussite ( $PbCO_3$ ), smithsonite ( $ZnCO_3$ ), or otavite ( $CdCO_3$ ) may form independently under ureolytic conditions, further enhancing immobilisation efficiency (Achal & Pan, 2014):

$$M^{2+} + CO_3^{2-} \rightarrow MCO_3$$
 (solid) (Equation 4)  
 $M^{2+} + CO_3^{2-} + nH_2O \rightarrow MCO_3 \cdot nH_2O$  (solid) (Equation 5)

Metals that do not enter the calcite lattice can still be immobilised by encapsulation within porous  $CaCO_3$  matrices (Xu et al., 2025). Moreover, the rise in pH during ureolysis facilitates the formation of metal hydroxides (e.g.,  $Cr(OH)_3$ ,  $Fe(OH)_3$ ,  $Zn(OH)_2$ ), further reducing solubility (Achal & Pan, 2014; Bian et al., 2024).

Organic-mediated immobilisation in EICP arises from interactions between metals and biomolecules in crude plant-derived urease extracts (e.g., soybean or swordbean). Functional groups (–SH, –COOH, –NH<sub>2</sub>) drive complexation, chelation, and sorption on organic matrices, while ligand exchange stabilises ions at proteinaceous or polysaccharide surfaces (Shu et al., 2022; Baffoe & Ghahremaninezhad, 2022; Chen et al., 2024). Biomolecules can also template CaCO<sub>3</sub> nucleation, altering morphology, phase stability, and crystallinity, with some ligands becoming occluded during growth (Addadi & Weiner, 1985; Baffoe & Ghahremaninezhad, 2022). Redox-active compounds (e.g., phenolics) may further reduce Cr<sup>6+</sup> to Cr<sup>3+</sup>, enhancing immobilisation (Dickinson et al., 2025). Collectively, these processes form a dynamic continuum of biomolecule-driven crystallogenesis spanning nucleation, growth modulation, and post-crystallisation reactions that shapes mineral reactivity and long-term stability (Weiner & Addadi, 2011; Chen et al., 2024).

## 2. Experimental Section

#### 2.1. Materials

Mineral precipitation in aqueous solutions containing nine different ecotoxic metals (EMs) - As, Cd, Co, Cr, Cu, Li, Ni, Pb, and Zn - was studied at 2 mM, 5 mM, and 20 mM. The experiment utilized a crude urease extract derived from soybeans (*Glycine max*), a 1 M solution of urea, and calcium chloride (CaCl<sub>2</sub>) as the calcium source. The soybeans were sourced from the Jalpur brand and purchased in a local supermarket, while the urea (98% purity) and metal salts (CdCl<sub>2</sub>, CoCl<sub>2</sub>, Cr<sub>2</sub>(SO<sub>4</sub>)<sub>3</sub>·xH<sub>2</sub>O, CuCl<sub>2</sub>, AsCl<sub>3</sub>, LiCl, NiCl<sub>2</sub>, PbCl<sub>2</sub>, and ZnCl<sub>2</sub>) were obtained from Sigma-Aldrich. All metal salts used were anhydrous and had a purity level of  $\geq$ 99.995%. For solution preparation, deionized water with a resistivity of 18.2 M $\Omega$ ·cm, provided by the Milli-Q ultrapure system in the University of Glasgow's Environmental Biogeochemistry laboratory, was employed. Full technical specifications and operational details for all equipment and methodologies used in this study are provided in the Supplementary Information.

### 2.1.1. Crude Urease Extract Preparation

To prepare the crude urease extract (CUE), 80 grams of whole soybeans were soaked in deionised water and blended to a total final volume of 1 L. After standing overnight at room temperature, the solution containing soybeans was processed using a Fridja f1900 masticating juicer (1 L capacity, 250 W) to separate solids from the liquid extract. To facilitate protein precipitation, calcium carbonate (CaCO<sub>3</sub>) was added to the extract, reaching an approximate concentration of 0.06 M. The mixture was allowed to settle for two hours, after which the supernatant was carefully decanted. This supernatant was then centrifuged at 3700 rpm for 15 minutes at 4° C and filtered through standard laboratory-grade filter paper (Grade 2) to obtain a clarified enzyme solution.

Urease activity was assessed following the method established by Whiffin (2004), with an average activity of  $2.66 \pm 0.7$  mM urea·min<sup>-1</sup>.

# 2.1.2. Preliminary Optimization of Soybean Concentration and Operational Parameters

The soybean extract concentration and operational parameters were optimized to determine the lowest soybean concentration that would achieve maximum calcium precipitation without excessive ammonium production. A series of tests were conducted, varying soybean extract concentrations (20, 40, 60, 80, and 100 g/L) and urea concentrations (0.25, 0.5, 0.75, and 1.0 M) to identify the ideal urease activity. The objective was to achieve sufficient urease activity to precipitate all the calcium in the precipitation solution without overproducing ammonium. This optimization led to an optimal soybean extract concentration of 80 g/L, corresponding to urease activity in the range of 2.66 mM urea·min<sup>-1</sup>. This level of urease activity was sufficient to fully precipitate all the calcium from the 1 M CaCl<sub>2</sub> solution in a precipitation solution composed of 1 M CaCl<sub>2</sub>, 1 M urea, and crude urease extract at a 1:1:1 ratio. This balance effectively prevented excessive ammonium production while ensuring complete precipitation. All experimental conditions were assessed in triplicate to ensure statistical reliability. Detailed information on the optimisation tests, including the method used to calculate urease activity, is provided in the Supplementary Information section.

## 2.2. Experimental Procedure

To evaluate metal immobilization by EICP, we prepared a solution by combining equal volumes (85 mL each) of (i) crude urease extract, (ii) an aqueous solution containing both the target ecotoxic metal (2 (T1), 5 (T2) or 20 mM (T3)) and 1 M CaCl<sub>2</sub>, and (iii) a 1 M urea solution. This mixture was aliquoted into five 50 mL Falcon tubes, incubated at 25 °C for 72 h, and then allowed to cure at room temperature for seven days. After curing, solids were rinsed with deionized water, collected on Grade 2 filter paper, and oven-dried at 37 °C for 24 h. Subsamples of the supernatant were taken for pH, conductivity, ammonium and metal concentration analyses, and dried precipitates were stored in airtight vials for subsequent SEM, EDS and XRD characterization.

#### 2.3. Assessment of Immobilization of EMs and Ammonium Production

The efficiency of the precipitation process in immobilizing ecotoxic metals (EMs) and ammonium was assessed by analysing the residual liquid. Solid particulates were first removed by filtering the liquid through Grade 2 filter paper (Whatman). A portion of the filtered liquid was then passed through 0.45  $\mu$ m syringe filters for ammonium determination. Ammonium concentration was measured using the salicylate colorimetric method, with analysis performed on a SEAL AutoAnalyzer (AA3). pH was recorded using a YSI ProDSS Multiparameter Probe, with recalibration conducted to

ensure consistency of readings at 25 °C. For metal concentration analysis, nitric acid (HNO<sub>3</sub>) was added to a separate aliquot of the filtered solution to achieve a final concentration of 2% (v/v). The metal content was quantified using Inductively Coupled Plasma Optical Emission Spectroscopy (ICP-OES) with a Thermo Scientific iCAP 7000.

### 2.4. Characterization of the Precipitates

The precipitates formed during the experiments were analysed as a single, powdery fine-grained fraction, with the size of the precipitates confirmed to be below 1 mm through visual observation. Scanning electron microscopy (SEM) was used to examine their morphology and size in detail. Powder X-ray diffraction (XRD) and Rietveld Refinement using Profex software (Doebelin & Kleeberg, 2015).

was performed on the entire precipitate sample to identify the primary mineral phases and quantify their relative proportions for each metal and treatment condition.

## 2.5. Sustainability and Circular Economy

# 2.5.1. Adaptive optimisation aligned with waste-to-resource, circular economy and GHG protocol principles

In this work we introduce adaptive optimisation as a novel framework for biogeotechnical remediation of soils and waters, defined as a continuous, feedback-driven process designed to improve pollutant removal efficiency while reducing energy, materials, labour and other inputs. This concept, applied here for the first time, embeds circular-economy and GHG Protocol principles by ensuring that sustainability gains are realised not only in the environmental outcomes but also in the practical and economic feasibility of the workflow.

Our approach applies adaptive optimisation to transform food-processing residues into functional reagents while reducing costs, energy consumption and greenhouse-gas emissions. Instead of relying on costly commercial preparations, we extract urease from soybean by-products, thereby upcycling waste streams and lowering material expenses.

Adaptive optimisation enabled us to streamline the process, replacing resource-intensive operations with simpler steps and achieving reductions in energy use, chemical demand and processing time. These refinements resulted in measurable reductions in energy demand, processing time and chemical inputs, alongside clear cost savings. In practice, adaptive optimisation was realised by continuously testing reagent concentrations and material quantities to maintain or improve removal efficiency while simultaneously reducing inputs. A concrete example is provided by the production of crude urease extract. Whereas commonly available protocols often prescribe multiple filtration steps and the use of ethanol and acetone for urease extraction, we employed only deionised water and a single filtration step. Despite this simplification, the resulting biomineral precipitation achieved an equivalent mass yield to that obtained through

more resource-intensive methods. Although commercial  $CaCl_2$  and urea were used in the present work for standardisation, both can be sourced from waste streams such as eggshells for calcium and urine for urea, thus paving the way towards fully circular EICP systems.

### 2.5.2. Greenhouse Gas Accounting and Comparative Emission Reduction

The comparative greenhouse gas (GHG) assessment was based on two laboratory-scale workflows: a representative Classical Method, constructed as a median model synthesising the most frequently reported soybean crude urease extraction protocols in the literature, and the Adaptive Optimisation Method developed in this study. Because reported classical protocols vary widely in duration, energy demand, and procedural complexity, the Classical Method used here represents a consolidated benchmark reflecting their average operational parameters.

To quantify the environmental gains achieved through adaptive optimisation, a GHG accounting comparison was performed between the Classical and Adaptive Optimisation Methods, normalised per litre of soybean crude urease extract (SCUE), in accordance with the Greenhouse Gas Protocol and ISO 14064-1:2018.

The adaptive workflow achieved a 54.4 % reduction in total  $CO_2$ e emissions (from 7.032 to 3.210 kg  $CO_2$ e  $L^{-1}$ ), primarily driven by decreased electricity consumption (Scope 2) of 59.1 % (3.397  $\rightarrow$  1.390 kg  $CO_2$ e  $L^{-1}$ ) and complementary Scope 3 reductions in employee commuting (50.0 %, 3.061  $\rightarrow$  1.531), upstream transport and distribution (50.0 %, 0.480  $\rightarrow$  0.240), and waste generation (46.8 %, 0.094  $\rightarrow$  0.050).

These findings confirm that laboratory-scale process optimisation can yield substantial carbon savings through combined energy, material, and time efficiencies. Full calculations, emission factors, and methodological details are presented in Annex A (Comparative GHG Report).

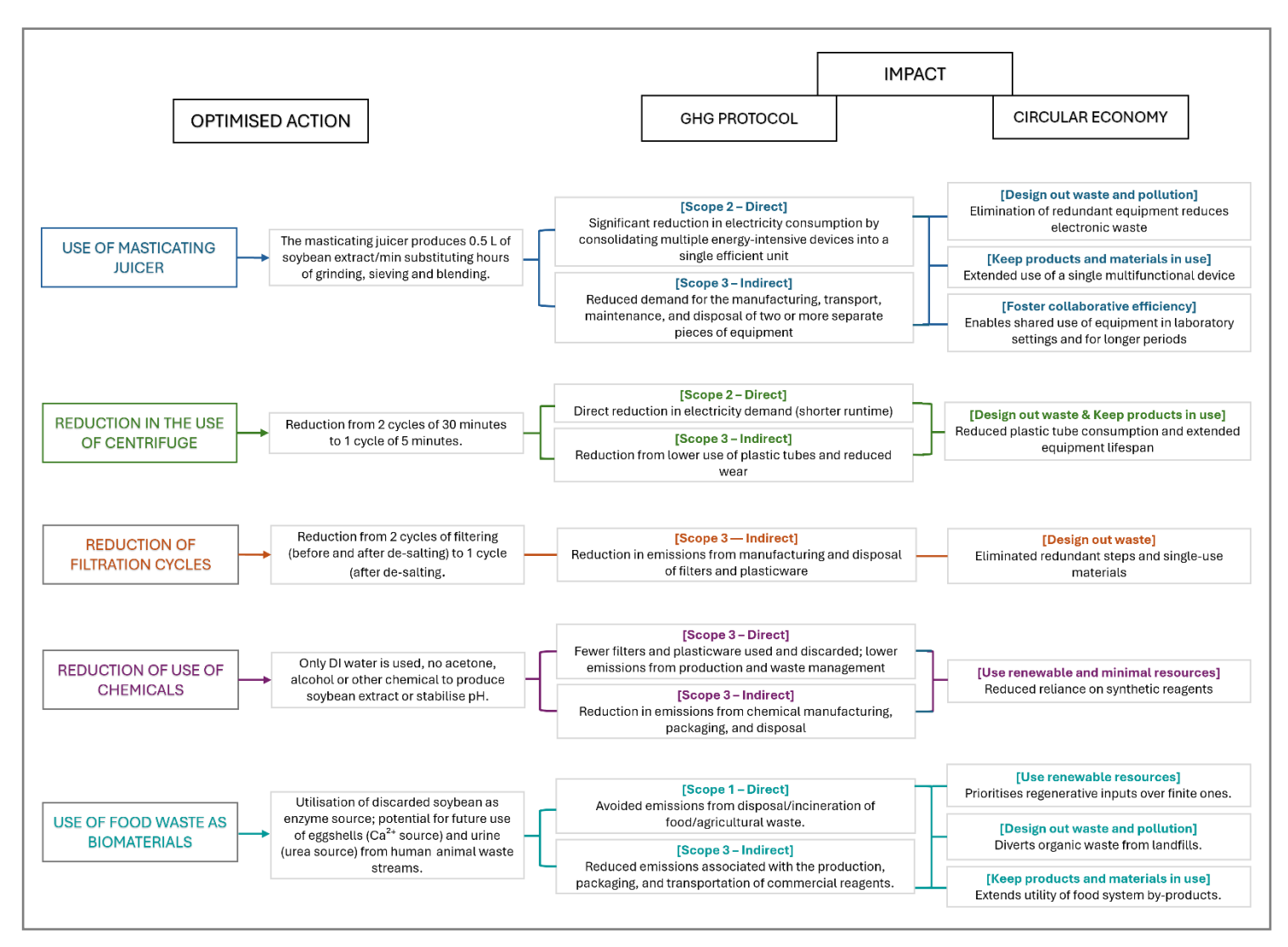


Figure 1 – Operational optimisation of crude urease extraction mapped against GHG Protocol scopes and circular economy principles. The diagram summarises key interventions introduced actions, integrating both direct and indirect emissions reductions under the GHG Protocol framework, alongside core principles of the circular economy.

#### 3. Results

### 3.1. System Response Parameters

To assess system behaviour across metal treatments, we quantified four core variables: final pH, ammonium concentration, precipitate mass, and metal removal efficiency. Together, these metrics provide an integrated view of ureolysis-driven alkalisation, carbonate generation, and overall immobilisation performance. We first report pH and ammonium as direct proxies of urease activity, followed by precipitate mass and removal efficiencies. Principal carbonate morphologies were assessed by scanning electron microscopy (SEM) to characterise precipitate crystal habits and textures.

## 3.1.1. pH and ammonium production measurements

The final pH and residual ammonium concentrations were measured after 72 hours to evaluate ureolytic activity and system alkalisation in the presence of each metal treatment (Figure 2). As ureolysis proceeds, the enzymatic hydrolysis of urea produces ammonium and hydroxide ions, resulting in a measurable rise in both pH and ammonium levels. Therefore, high values for both parameters are indicative of efficient urease activity, whereas reductions reflect enzymatic inhibition.

The control sample, which received no metal addition, exhibited the highest final pH (approximately 8.4) and ammonium accumulation around 3,800 ppm, representing unhindered ureolysis for this system in the absence of inhibitory effects. In contrast, metal-treated systems displayed variable reductions in both parameters, reflecting differing degrees of interference with enzymatic function and carbonate precipitation.

Among all treatments, Cu<sup>2+</sup> and As<sup>3+</sup> exerted the strongest inhibitory effects, as evidenced by their consistently low final pH values (ranging from 6.5 to 7.0) and ammonium concentrations below 1,500 ppm. These findings indicate that ureolysis was substantially suppressed in the presence of these elements at the tested concentrations.

Cr<sup>3+</sup> and Cd<sup>2+</sup> showed moderate inhibition, with final pH values between 7.8 and 8.1 and ammonium concentrations between approximately 2,000 and 2,500 ppm, suggesting partial retention of urease activity. A slight downward trend in both parameters was observed across treatments T1 to T3 for these metals.

By comparison, Co<sup>2+</sup>, Li<sup>+</sup>, Ni<sup>2+</sup>, Pb<sup>2+</sup> and Zn<sup>2+</sup> maintained high final pH values (around 8.0 to 8.3) and elevated ammonium concentrations between 3,200 and 3,600 ppm, closely approaching those of the control. These results indicate that ureolytic activity remained largely unaffected in these systems, and any inhibition was minimal.

Overall, the data reveal a clear metal-specific pattern of urease inhibition, with Cu<sup>2+</sup> and As<sup>3+</sup> markedly impairing activity, Cr<sup>3+</sup> and Cd<sup>2+</sup> producing moderate effects, and the remaining metals, particularly Li<sup>+</sup>, Zn<sup>2+</sup> and Pb<sup>2+</sup>, exerting negligible impact under the tested conditions.

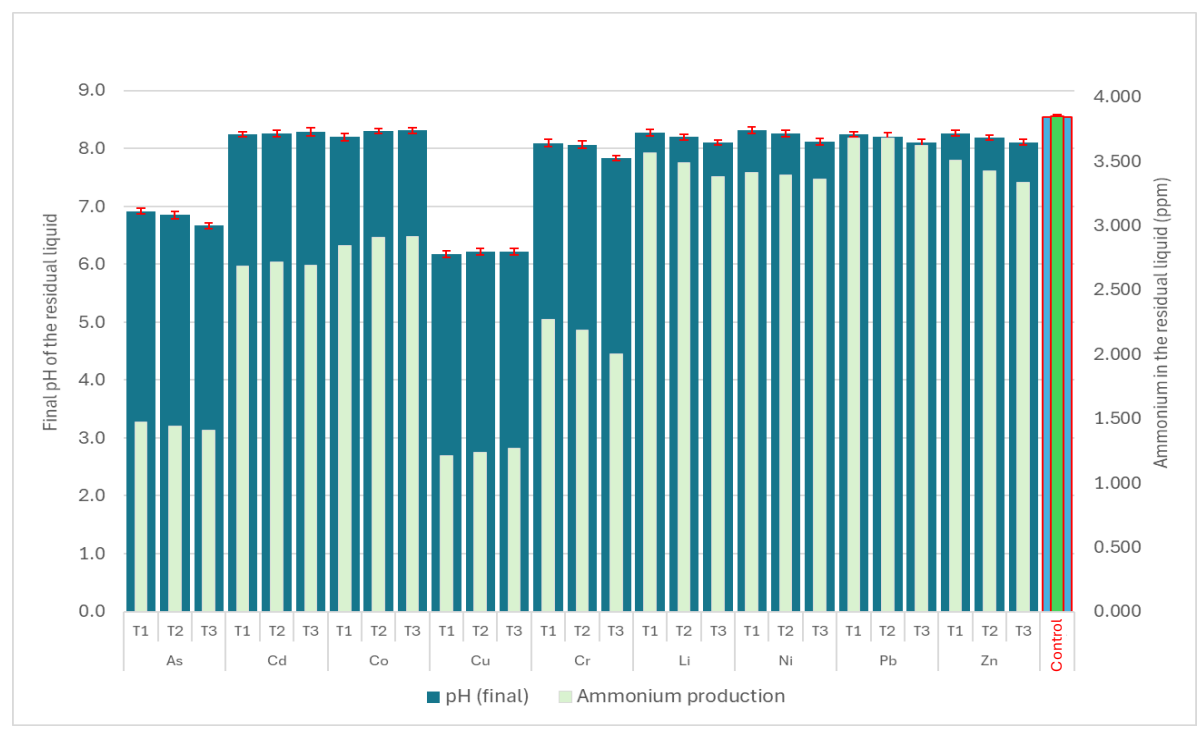


Figure 2. Final pH (blue bars) and residual ammonium concentration (green bars) measured after 72 hours of incubation in each metal treatment with N=5 for pH and N=1 for ammonium release. Initial pH =  $6.8 \pm 0.4, 25$  °C.

### 3.1.2. Precipitate mass

Gravimetric analysis of the precipitates formed during the enzyme-mediated treatment process revealed distinct patterns in the mass of solids recovered per metal species across treatments T1 to T3. Figure 3 exhibits the measured values for each metal per treatment plus control.

Arsenic and copper exhibited consistently low precipitation across all treatments, with values remaining markedly below the control. Arsenic decreased slightly from 0.43 g in T1 to 0.40 g in T3, showing a minor but consistent reduction. Copper fluctuated modestly, increasing from 0.43 g in T1 to 0.47 g in T2, then returning to 0.44 g in T3, reflecting minimal net change. Both elements showed low overall precipitation and limited responsiveness to treatment variation.

Cobalt exhibited a moderate precipitation profile with 0.62 g in T1, 0.65 g in T2, and a slight decrease to 0.53 g in T3, reflecting overall stability with minor variation under treatment conditions.

Cadmium, chromium, nickel and zinc displayed higher degrees of variability. Cadmium decreased substantially from 1.80 g in T1 to 0.44 g in T3, with a sharp decline observed between T2 and T3. Chromium showed a marked reduction from 1.78 g in T1 to 0.45 g in T3, with a large drop already evident by T2. Nickel initially presented elevated mass in T1 (1.70 g), followed by a substantial decline to 0.52 g in T2 and 0.40 g in T3, suggesting a pronounced downward trend. Zinc exhibited a similar pattern, decreasing from 1.78 g in T1 to 0.58 g in T3, with the most notable change occurring between T2 and

T3. These elements demonstrated high initial precipitation followed by sharp reductions, indicative of treatment-sensitive behaviour.

In contrast, lithium and lead consistently produced the highest masses among all tested elements. Lithium remained nearly constant across treatments, with 1.73 g in T1, 1.76 g in T2, and 1.79 g in T3, indicating extremely stable and elevated precipitation. Lead also exhibited minor variation, increasing slightly from 1.77 g in T1 to 1.80 g in T3. Both elements closely approached the mass observed in the control (1.82–1.85 g), suggesting robust and sustained precipitation with minimal sensitivity to treatment modifications.

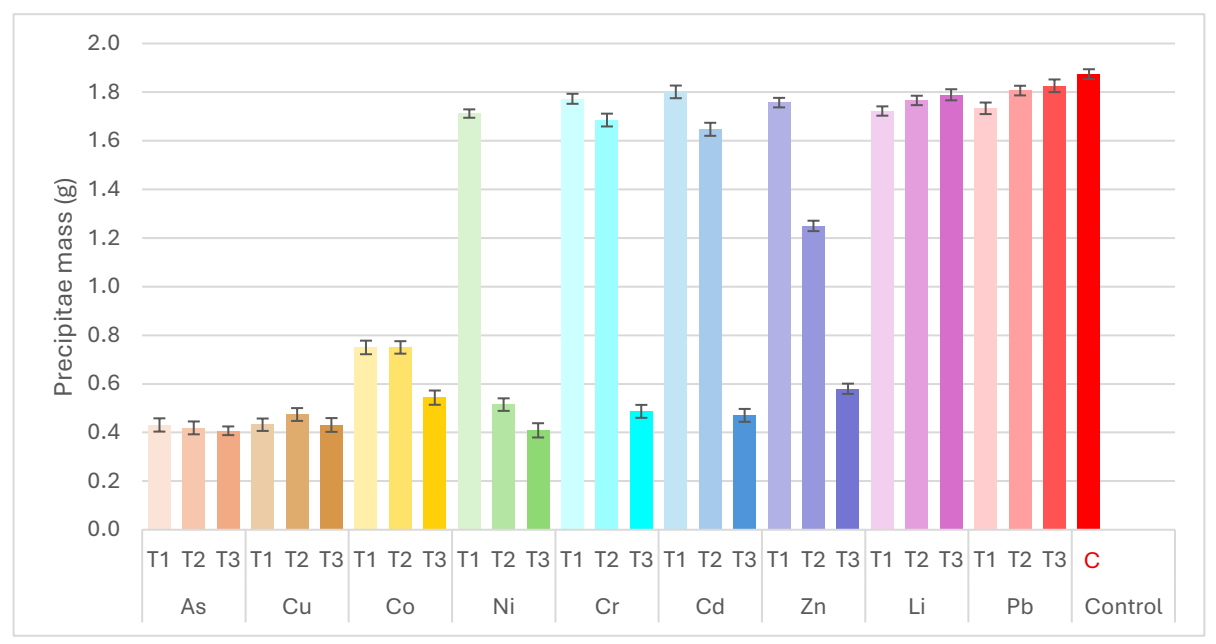


Figure 3. Mass of solid precipitate for each metal treatment (T1–T3) and control (A–C). Bars represent mean precipitate mass  $(g) \pm standard deviation (N = 5)$ .

## 3.1.3. Ecotoxic metals removal efficiency

The removal efficiencies of individual metals across treatments T1, T2, and T3 are summarised below in Figure 4, providing a basis for comparative analysis of element-specific performance and inter-treatment variability. Removal efficiencies across all tested metals showed consistently high values, generally above 70%, though distinct patterns were evident among metals. Based on average removal percentages across treatments T1, T2, and T3, the metals could be grouped into four efficiency categories.

Lead, cobalt, cadmium and nickel exhibited the highest removal efficiencies, consistently reaching values between 93% and 99% across all treatments, indicating nearly complete removal and exceptional process performance. Zinc and chromium followed, maintaining efficiencies between approximately 86% and 98%, with modest variation among treatments reflecting kinetic and redox sensitivity. Lithium presented slightly lower but still high removal values, ranging between 89% and 92%, demonstrating stable yet moderately sensitive behaviour to treatment conditions. Copper and arsenic displayed the lowest efficiencies in this study, with copper averaging about 88% and

almost no variation between treatments and arsenic remaining around 75–77% across all treatments, marking them as comparatively less responsive elements in the system.

In terms of stability across treatments, lead, cobalt and copper showed negligible variation. Lithium and arsenic were also highly consistent (≤ ~1-3 percentage points). Cadmium decreases 4 points between T1 and T3 Zinc and nickel exhibited clearer intertreatment changes: zinc decreased by 11 points from T1 to T3, and nickel dropped by 5 points from T1 to T3. Chromium exhibited the larger decrease between T1 and T3, circa 13 points.

Overall, these findings indicate broadly high removal across all metals, with Pb, Cr, and Zn showing the highest and most stable efficiencies, Cd, Co, and Ni maintaining consistently strong performance with minor variation, Li presenting moderate but reliable removal, and Cu and As displaying the lowest overall efficiencies, though still achieving substantial immobilisation within the system.

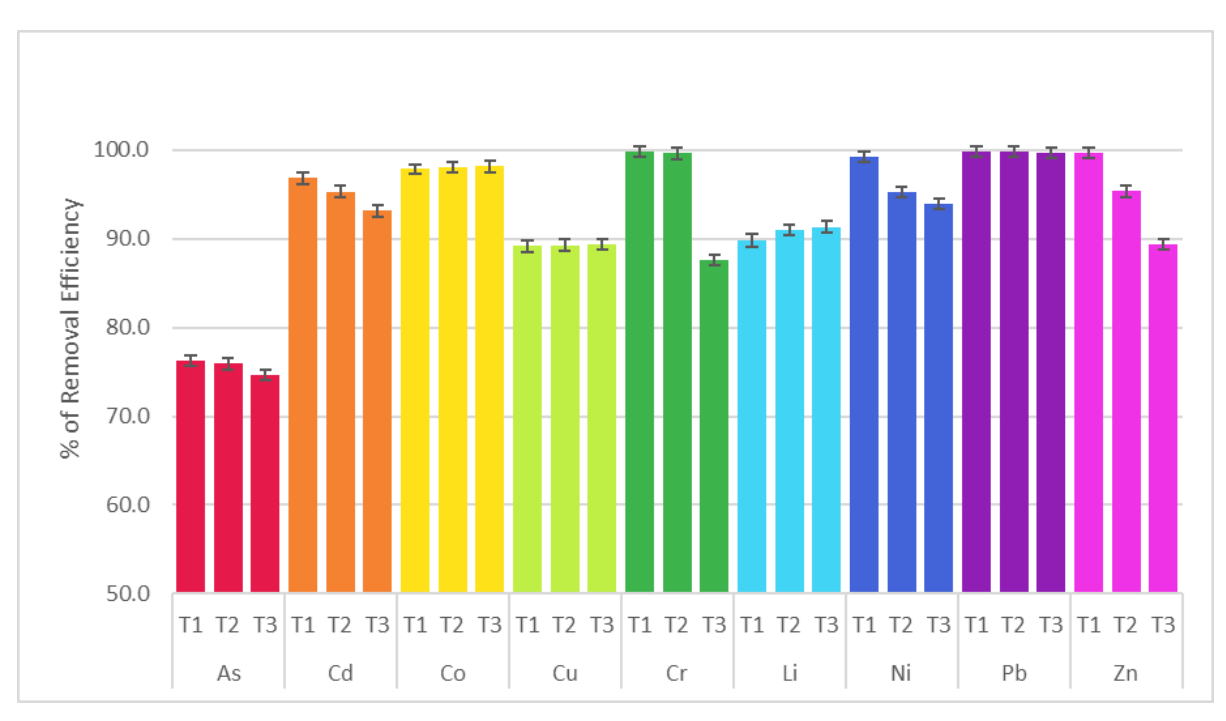


Figure 4. Metal removal efficiency (%) after 72 hours for each treatment (T1–T3) across all tested elements. Bars represent mean values  $\pm$  standard deviation (N = 5).

# 3.2. Morphological and Microtextural Characterisation of Mineralogical Assemblages

All SEM micrographs were acquired at a consistent magnification, with image scales fixed at  $20\,\mu m$  to ensure visual comparability across treatments (Figure 5). Carbonate precipitates in the control samples predominantly occur as spheroidal aggregates. These are observed as isolated particles, clustered groups of smaller spheres, or as paired spheroids forming composite aggregates. In many cases, spheroids are surrounded by a coarser outer overgrowth, producing a distinct core—shell texture (hereafter referred to as sunflower texture, indicated with letter S in Figure 5), where a spheric inner core with smooth surface is enveloped by a radially crystalline crust marked

by dense coverage of nanometric protrusions or microcrystalline granules, imparting a distinctly roughened appearance. Detachment of the inner sphere occasionally results in circular voids, indicating that the core and crust represent structurally distinct growth domains (Figure 5 Control 1, 2 and 3). In addition to these features, clusters of microspheres are commonly embedded within, or coalesced into, more massive carbonate phases with relatively smooth and continuous surfaces, lacking defined substructures (indicated as M in Figure 5 control samples). These compact morphologies contrasted sharply with the granular and radial features described above, indicating a broader diversity in precipitation habits even under control conditions.

Samples treated with Zn, Li, and Pb exhibited morphologies broadly comparable to the control, with similar combinations of spheroidal, sunflower-like, and dense granular forms (Figure 5 Zn, Li and PB T1, T2 and T3). Minor variations were observed in crystal size and packing density across treatments. In Pb-treated samples, however, aggregates sometimes adopted a distinctive bone-like appearance, composed of interlocking, elongated structures with porous, trabecular textures (Figure 5 Pb T1 and T3, indicated with letter B). This represented a subtle but consistent shift in crystal organisation.

Chromium-treated samples revealed a marked progression in carbonate morphologies across the experimental series. At T1, precipitates were dominated by aggregates with a distinctly crystalline habit, composed of well-developed faceted units intergrown into compact clusters and spheroids with rugged superficial microtexture. At T2, spheroidal morphologies became more abundant, often forming dense clusters and partially coating earlier crystalline fragments, indicating a shift towards rounded growth forms. By T3, the precipitates were largely composed of irregular, poorly defined aggregates with a more porous or lamellar character, lacking the sharp crystalline outlines observed at T1. This transition from faceted crystalline structures to spheroidal and ultimately less defined morphologies suggests that chromium exerts a strong control on carbonate growth pathways, progressively favouring disordered and less crystalline habits over time.

Nickel-treated samples also displayed a clear transition in carbonate morphologies through the experimental sequence. At T1, precipitates were dominated by spheroidal particles, which frequently occurred in dense clusters and in some cases fused into larger aggregates. At T2, spheroidal morphologies remained abundant, but they were increasingly associated with irregular granular overgrowths and intergrown fragments, giving rise to more heterogeneous clusters. By T3, the assemblage was characterised by the predominance of blocky to tabular aggregates, composed of equant carbonate crystals with well-developed planar surfaces and sharp edges. This progression from spheroidal to blocky morphologies indicates that, at higher concentrations, Ni appears to disfavour well-ordered crystallization, instead promoting the development of blocky aggregates with poorly defined crystalline surfaces.

Cobalt-treated samples displayed a diverse range of morphologies that shifted systematically with concentration. At low concentration (T1), carbonates formed irregular compact aggregates with limited surface definition. Intermediate concentration

(T2) promoted the appearance of spheroidal particles with striking trigonal faceted surfaces, composed of finely lamellar subunits that produced delicate filigree-like textures. At the highest concentration (T3), cobalt favoured the development of abundant spheroids, which occurred in densely packed clusters with smoother surfaces compared with the faceted forms of T2. This progression suggests that cobalt strongly influences carbonate habit, enhancing spheroidal growth while modulating the expression of faceted versus rounded surfaces.

Cadmium-treated samples showed a clear preference for faceted over spheroidal morphologies. At low concentration (T1), precipitation was dominated by sharp, blade-like and tabular crystals that intergrew into compact, highly angular aggregates. Intermediate concentration (T2) preserved this faceted habit but also introduced blocky masses with smooth, fractured surfaces, alongside occasional lamellar forms. At the highest concentration (T3), the products remained largely crystalline and faceted, with dense granular clusters replacing the spheroidal aggregates so typical of the controls. Overall, cadmium strongly favoured the development of angular, intergrown crystals and suppressed the formation of rounded spheroidal morphologies, setting it apart from most other treatments.

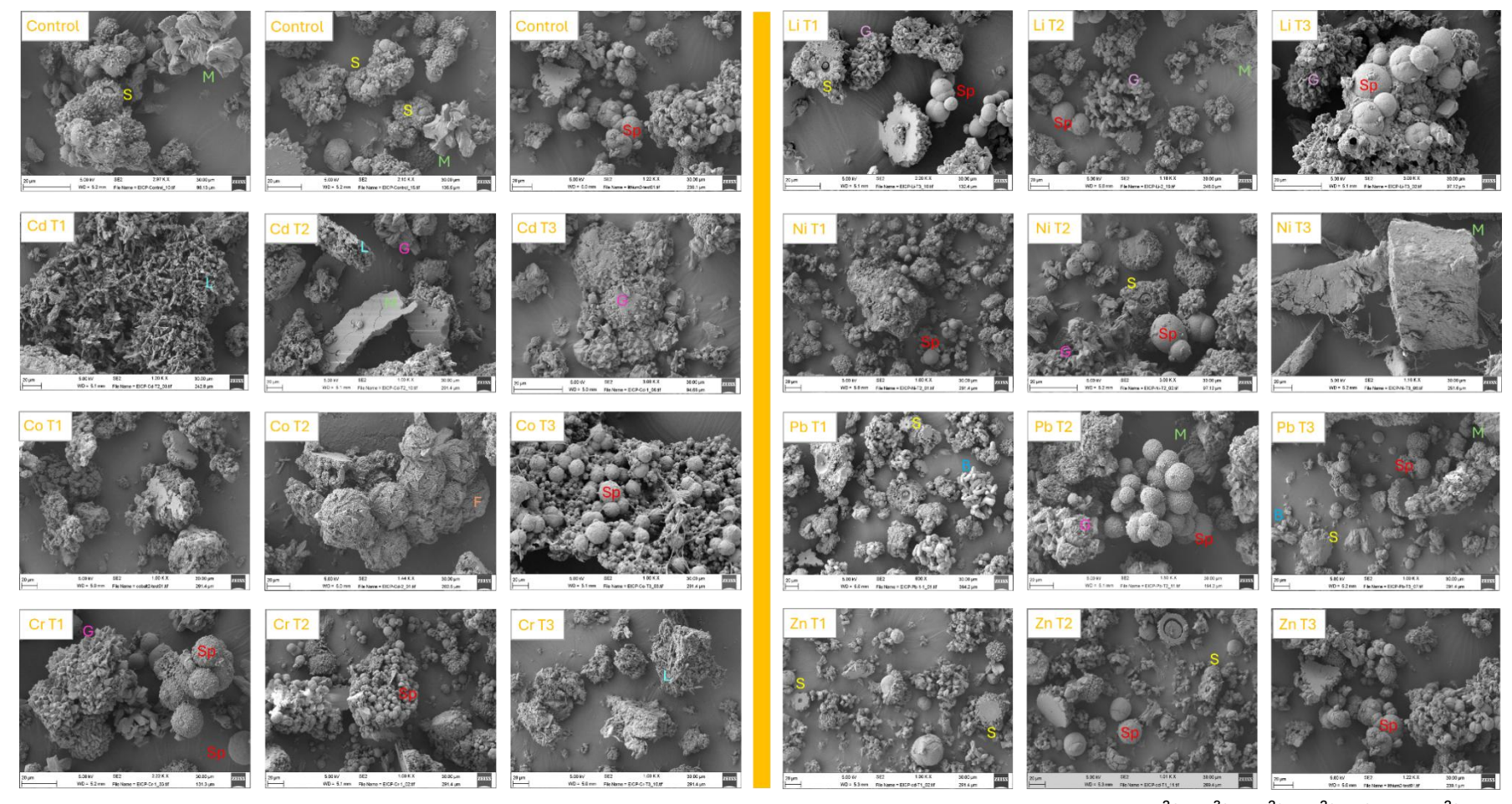


Figure 5. Scanning electron micrographs (SEMs) of precipitates recovered from the EICP experiments with nine metal ions ( $Co^{2+}$ ,  $Cr^{3+}$ ,  $Cd^{2+}$ ,  $Pb^{2+}$ ,  $Li^+$ , and  $Ni^{2+}$ ) across three treatment levels (T1, T2, T3), alongside control conditions without metal addition, revealing substantial morphological diversity in carbonate-based precipitates. Legend of the textures present in the images: B – bone-like (blue); F – Filigree like superficial texture on spheroidal carbonate; G - granular polyhedral (pink); L - lamellar or platey-like (aqua-blue); Sp = Spherical (red); S – sunflower-like (yellow); M = massive texture (green).

# 3.3. X-Ray Diffractometry and Semi-Quantitative Phase Analysis by Rietveld Refinement

The XRD patterns confirm consistent calcite formation across all treatments analysed, with variations in peak sharpness and angular position, most notably around the (104) reflection (Figure 6A, B). Arsenic and copper treated residues were not analysed due to insufficient recovered mass, as the fine precipitates remained embedded within the filter paper rather than forming separable solids. This likely indicates the presence of poorly crystalline or amorphous phases that resisted recovery under the tested conditions.

All analysed samples display calcite as the dominant crystalline phase, although subtle differences in reflection symmetry and intensity indicate varying degrees of crystallinity. Broader and less intense peaks in the Ni T1 and Co T1 treatments suggest comparatively lower crystallinity, while sharper reflections in Ni T2 and Co T2 indicate slightly improved ordering. Across most metals, T1 treatments yielded narrower peak bases than T2, suggesting that higher metal loadings may inhibit calcite crystal growth; the Ni series presented the opposite trend.

In addition to calcite,  $Pb^{2+}$  promoted the formation of cerussite ( $PbCO_3$ ) in estimated proportions of 2–4 wt % (T1–T3), while  $Cd^{2+}$  produced traces (< 0.5 wt %) of otavite ( $CdCO_3$ ). Although cerussite was consistently identified by Rietveld refinement, its diagnostic peaks are obscured within dominant calcite reflections. This likely reflects its occurrence as a minor phase near the 5 wt % detection limit, peak overlap, and possible broadening from nanocrystalline or partially substituted domains. The semi-quantitative phase estimates should therefore be regarded as approximate indicators of relative abundance.

Magnified inspection of the (104) reflection (Figure 6B) revealed systematic angular displacements relative to the control. The control sample itself exhibits a slight shift to lower angles compared with the standard reference for pure calcite (29.40° 20), attributed to organic incorporation during biomineralization. Among the treated residues, the Cr-treated sample showed the largest displacement ( $\Delta 2\theta \approx -0.10^{\circ}$ ), followed by Li and Ni ( $\approx -0.07^{\circ}$ ), whereas Zn, Pb, and Cd exhibited moderate shifts ( $-0.03^{\circ}$  to  $-0.05^{\circ}$ ). In contrast, the Co-treated sample shifted marginally to higher angles ( $+0.02^{\circ}$ ), corresponding to the smallest d-spacing among all treatments. The observed order of displacement magnitude, Cr > Li  $\approx$  Ni > Zn > Pb > Cd > Control > Co, suggests progressive lattice contraction or expansion depending on the effective ionic radius and substitutional potential of each metal. Contraction (positive  $\Delta 2\theta$ ) indicates replacement by smaller or more strongly bonded cations, while expansion (negative  $\Delta 2\theta$ ) implies substitution by larger or weakly bound ions within the calcite lattice.

The SEM observations align with these crystallographic signatures. Group I metals (Ni, Zn, Pb) produced well-defined calcite aggregates with characteristic sunflower or spherulitic morphologies, indicative of vaterite-to-calcite transformation and partial lattice substitution. Group II metals (Cr, Fe, Mn) yielded irregular, faceted, or fused grains consistent with surface adsorption and limited structural incorporation. Conversely,

Group III metals (Cu, As) generated sparse, poorly developed precipitates, consistent with urease inhibition and incomplete carbonate mineralisation. Collectively, the XRD and SEM evidence delineate a continuum from substitutional incorporation to enzymatic suppression, linking metal-specific crystallographic behaviour directly to the biochemical dynamics of the EICP process.

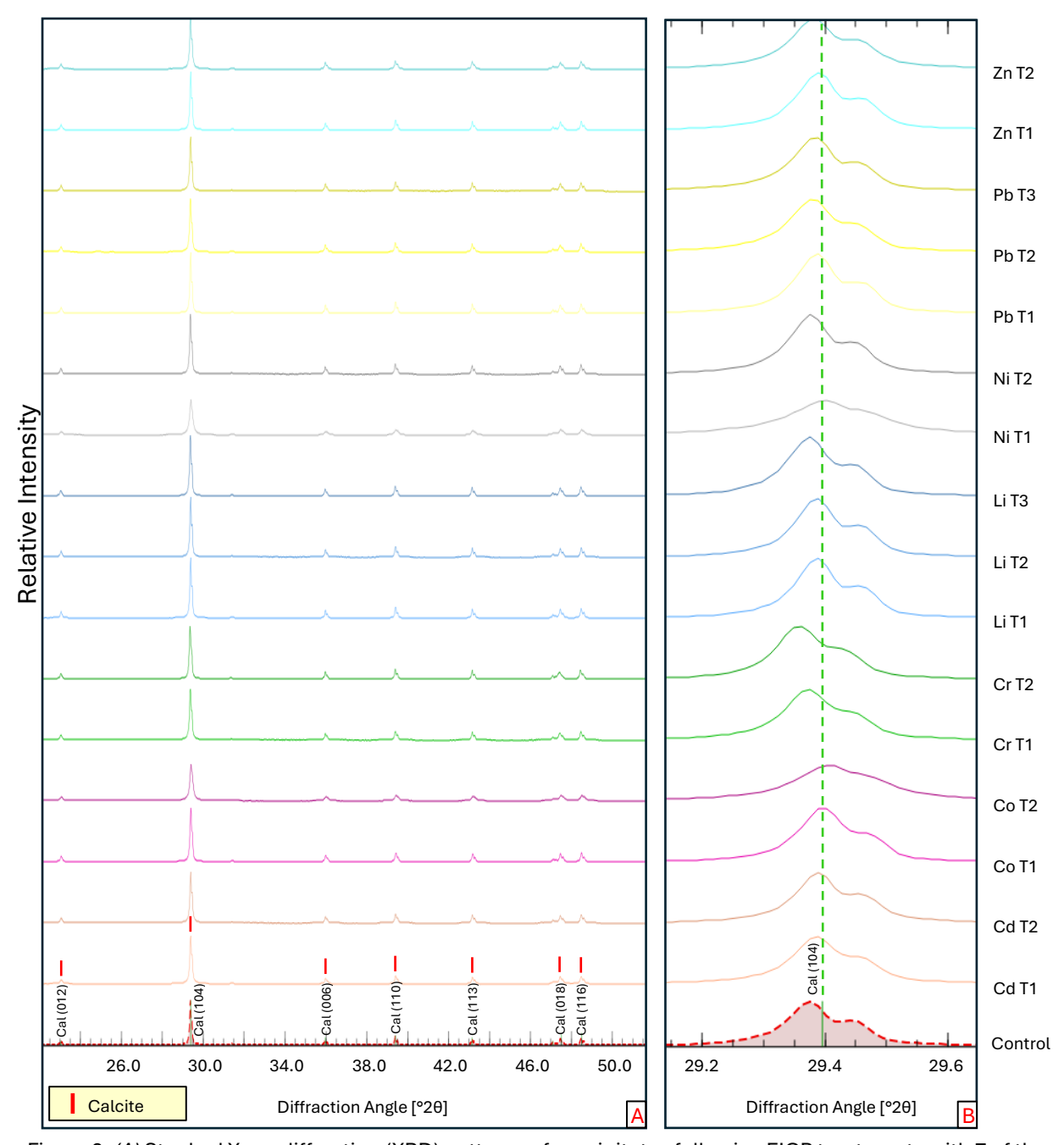


Figure 6. (A) Stacked X-ray diffraction (XRD) patterns of precipitates following EICP treatments with 7 of the 9 ecotoxic metals. Red markers indicate the main reflections of calcite (PDF 05-0586), confirming its predominance across all samples. (B) Magnified view of the calcite (104) reflection, with a green dashed line marking the standard reference position at  $20 \approx 29.40^{\circ}$ . The control sample is exhibited at the bottom with a red dash line.

### 4. Discussion

### 4.1. Pathways of metal uptake by mineralisation

Under enzyme-induced carbonate precipitation (EICP), metal immobilisation arises from the coupled influence of lattice compatibility, coprecipitation kinetics, and aqueous speciation–redox dynamics, which together determine whether metals are incorporated into the calcite lattice or retained as adsorbed or secondary carbonate phases (Reeder, 1996; Putnis & Putnis, 2007; Fang et al., 2022). Metals were classified by immobilisation efficiency and mechanistic stability across treatments, revealing three behavioural groups that capture distinct uptake mechanisms and sensitivities to EICP conditions. Group I (Pb, Cd, Co, Ni) achieved the highest and most consistent removal (93–99%), reflecting strong lattice affinity and stable coprecipitation. Group II (Cr, Zn) also reached high efficiencies (86–99%) but exhibited greater sensitivity to alkalisation and precipitation kinetics. Group III (Li, Cu, As) showed lower and more variable removal (70–92%), dominated by adsorption, sectoral entrapment, or limited carbonate precipitation.

# 4.1.1. Group I (Pb, Cd, Co, Ni): Robust immobilisers — lattice-compatible metals (substitution/coprecipitation dominance)

Pb, Cd, Co and Ni share key geochemical traits: divalent charge, carbonate affinity, and the capacity to substitute for Ca<sup>2+</sup> within the calcite structure, making them among the most structurally compatible trace metals in carbonate systems despite differences in ionic radius (Rouff et al., 2002; Andersson et al., 2014; McBride, 1980; Reeder, 1996; Stipp et al., 1992; Freij et al., 2004; Lakshtanov & Stipp, 2007; González-López et al., 2014). Their retention is governed primarily by substitutional and coprecipitation processes, yielding immobilisation states that range from true lattice incorporation to limited carbonate segregation (Reeder et al, 1999; Sturchio et al., 1997; Rouff et al., 2005; Andersson et al, 2014).

Lead exhibits a strong structural affinity for carbonate minerals, driven by its low hydration energy and its near-ideal charge and size compatibility for Ca<sup>2+</sup> substitution (Andersson et al., 2014).

During mineral growth, Pb is incorporated through substitution and coprecipitation at the calcite-water interface, preferentially occupying step and kink sites along {104} faces where local coordination is most flexible (Sturchio et al., 1997; Callagon et al., 2014). In parallel, first-principles simulations show that Pb binds strongly to hollow and bridge sites on the calcite (104) surface and tends to form stable Pb clusters at higher surface coverages, reinforcing its high affinity for carbonate substrates (Wang et al., 2022). In situ AFM and X-ray reflectivity studies have shown that this process yields strained but coherent Pb-calcite solid solutions (Sturchio et al., 1997; Fenter et al., 2000), while atomistic models identify carbonate-terminated hollow sites as the most stable adsorption configuration (Wang et al., 2022). In our experiments, ureolysis

remained fully active in the presence of Pb (final pH > 8.1;  $[NH_4^+]$  > 3,300 ppm), leading to near-complete removal (>99%) and the formation of abundant calcite with minor cerussite (2–4%). The moderate shift of the {104} reflection to lower 20 indicates lattice distortion consistent with Pb substitution, and the trabecular to sunflower-like morphologies reflect Pb-modulated growth along active crystal faces. Despite the relatively low enzymatic activity of our crude urease extract, the evolution of Pb removal, pH and carbonate mineralogy is consistent with other crude-urease EICP systems (Wang et al., 2022; Xu et al., 2025), supporting Pb's high structural compatibility and kinetic stability in EICP environments.

Cadmium behaves as a near-ideal divalent substitute for Ca<sup>2+</sup> in calcite due to its close ionic-radius match and compatible coordination environment (McBride, 1980). Experimental and spectroscopic studies show that Cd<sup>2+</sup> is readily taken up at step edges and defect-rich sites, forming epitaxial CdCO<sub>3</sub> coatings and progressively evolving into calcite-otavite solid solutions (Stipp et al., 1992; Callagon et al., 2017). The stability of these mixed carbonates and the ease of Cd incorporation into the lattice are further supported by thermodynamic and structural analyses of the  $(Ca_{1-x}Cd_x)CO_3$  series (Ma et al., 2022). Under increasing supersaturation, Cd transitions from initial surface binding to the formation of mixed Ca-Cd carbonate phases, with XRD and XPS evidence for Ca<sub>0.67</sub>Cd<sub>0.33</sub>CO<sub>3</sub> and other otavite-like domains (Lee, 2025; Ma et al., 2022). These mixedcarbonate phases reflect short-range ordering and partial solid-solution behaviour typical of Cd incorporation into the calcite lattice. Geochemical and spectroscopic studies identify two complementary regimes: at pH ≥ 7.9, CdCO<sub>3</sub> precipitation contributes directly to removal (Davis et al., 1987; Lee, 2025), whereas at higher Cd activities, chemisorptive substitution and the formation of Ca-Cd carbonate solid solutions become dominant (Stipp et al., 1992; Ma et al., 2022). In our system, removal exceeded 95%, with pH  $\approx$  7.8–8.0 and  $[NH_4^+] \approx$  2,500 ppm indicating sustained ureolysis but moderated carbonate yield. The sharp reduction in precipitate mass from T1 to T3 likely reflects slower nucleation kinetics and reduced coprecipitation efficiency rather than enzymatic inhibition. XRD shows moderate lattice expansion and well-defined reflections consistent with otavite-like incorporation and limited structural disorder, confirming substitutional uptake under high supersaturation typical of EICP environments.

Nickel and cobalt exhibited comparable removal efficiencies (93–98%), supported by sustained ureolysis (pH > 8.0;  $[NH_4^+] \approx 3,000$  ppm) and the formation of crystalline calcite. Despite similar retention, their incorporation pathways diverged mechanistically. Nickel displayed broad but coherent incorporation into the calcite lattice. At near-neutral to alkaline pH, Ni<sup>2+</sup> forms inner-sphere surface complexes with carbonate groups and step edges, which progressively evolve into solid solutions as growth advances (Lakshtanov & Stipp, 2007). Density-functional theory demonstrates that Ni-for-Ca substitution in calcite is energetically favourable, generating local relaxation around the defect rather than purely radius-controlled distortion (Andersson et al., 2014). The modest shift of the {104} reflection to lower 20 is consistent with this strain field, indicating coherent incorporation mediated by defect-assisted substitution.

SEM shows that low Ni activities produce smooth, spheroidal aggregates, whereas higher loadings yield granular to blocky morphologies, reflecting strain accumulation in Nienriched growth sectors. Together with the inner-sphere surface complexes observed at near-neutral to alkaline pH (Lakshtanov & Stipp, 2007), these features indicate a coupled adsorption–substitution pathway in which Ni-bound surface sites are progressively buried during overgrowth, forming compositionally zoned but structurally coherent (Ca,Ni)CO $_3$  domains.

Cobalt, by contrast, produced roughly half the precipitate mass recovered in the Ni treatments, suggesting a stronger inhibition of carbonate growth. AFM studies show that Co<sup>2+</sup> can perturb step kinetics on calcite, stabilising early growth layers but suppressing step propagation, resulting in surface enrichment rather than deep incorporation (Freij et al., 2004; Xu et al., 2015; Riechers et al., 2022). In our samples, the {104} reflection shifted slightly to higher 20, implying lattice contraction consistent with limited Co substitution in calcite and with the strongly non-ideal behaviour of the (Co,Ca)CO<sub>3</sub> solid solution (Katsikopoulos et al., 2008). The broader and less intense reflections at T2 correspond to lower crystallinity, consistent with non-ideal mixing and strain at Co-rich boundaries and/or associated hydroxy-carbonate domains (Katsikopoulos et al., 2008; Xu et al., 2015; Riechers et al., 2022). SEM microtextures reveal spheroidal aggregates with trigonal–lamellar surfaces, particularly at intermediate concentration, reflecting adsorption-controlled growth and sectoral overgrowth rather than full solid-solution formation (González-López et al., 2016; Riechers et al., 2022).

# **4.1.2.** Group II (Zn, Cr): Mixed-control metals — substitution possible but strongly modulated by kinetics/redox

Metals in this group exhibit an intermediate regime between structural compatibility and chemical exclusion. Their partial substitutional capacity is counterbalanced by stronger kinetic and aqueous constraints, where precipitation rate, complexation, and redox speciation dictate retention pathways. Under EICP conditions, this manifests as a transition from defect-assisted incorporation to surface-controlled precipitation.

Zinc illustrates this mixed behaviour. Its smaller ionic radius (0.74 Å) relative to  ${\rm Ca}^{2+}$  (1.00 Å) is expected to impose local lattice strain during substitution, which likely favours incorporation in locally distorted environments rather than an ideal, fully ordered calcite lattice. Spectroscopic studies indicate that Zn in calcite-related environments adopts a distorted, approximately octahedral coordination with oxygen, consistent with isomorphic substitution at Ca sites under non-ideal local geometry (Reeder et al., 1999; Elzinga et al., 2006). In this study, Zn retention reached 95–97%, coincident with efficient ureolysis (pH > 8.0;  ${\rm [NH_4^+]} \approx 3,000$  ppm) and extensive carbonate precipitation. Moderate shifts of the {104} calcite reflection, together with spheroidal to sunflower-like crystal morphologies, are consistent with crystallographically influenced Zn coprecipitation at relatively low substitution levels, rather than formation of a highly Zn-rich, metastable calcite. The strong dependence of Zn retention on the rate and extent of alkalisation is

therefore consistent with Zn occupying an intermediate position between true latticeforming cations and dominantly surface-bound species in EICP systems.

Chromium, by contrast, operates under redox and hydrolysis control (Islam et al., 2023). Its low structural compatibility with calcite, combined with the propensity of Cr(III) to form hydroxide complexes, limits substitutional uptake almost entirely (Rai et al., 2007; Garcia-Sanchez & Alvarez-Ayuso, 2002; Fang et al., 2022). Although overall Cr retention exceeded 85%, higher Cr loads inhibited ureolysis and suppressed carbonate yield (pH < 8.0;  $[NH_4^+] \approx 1,800-2,200$  ppm), producing fine-grained, lamellar, and poorly ordered morphologies. XRD revealed pronounced {104} displacements, the largest among all treatments, consistent with lattice distortion driven by surface-bound Cr or organic interactions. These traits indicate that Cr is immobilised primarily through adsorption and surface precipitation of  $Cr(OH)_3$ -like phases, with minimal lattice incorporation. The result is a redox-sensitive immobilisation pathway that couples strong inhibition of carbonate growth with partial loss of crystallinity in the precipitate.

# 4.1.3. Group III (Li, Cu, As): Alternative-pathway immobilisers — non-classical pathways (adsorption, sectoral entrapment, limited precipitation)

Ecotoxic metals and metalloids in this group follow non-classical immobilisation pathways, governed by adsorption, sectoral entrapment, or surface precipitation rather than direct lattice substitution. Their interaction with carbonate phases is largely chemical, reflecting the dominance of charge balance, hydration energy, and redox reactivity over crystallographic control. The resulting products are often amorphous or poorly ordered, and their formation frequently coincides with partial inhibition of ureolysis.

Among these, lithium achieved the highest retention (89–92%), coupled with efficient ureolysis (pH > 8.0;  $[NH_4^+] \approx 3,000$  ppm) and abundant carbonate yield (1.6–1.9 g). The resulting calcite exhibited sunflower-like morphologies also observed in control samples, which indicate growth dominated by {104} faces rather than a Li-specific effect. However, the measurable shifts in the {104} reflection in Li-treated samples point to subtle lattice perturbations consistent with minor Li incorporation. Rather than substituting directly for  $Ca^{2+}$ ,  $Li^+$  is likely accommodated through epitaxial coincidence between calcite and zabuyelite-like ( $Li_2CO_3$ ) domains, enabling local charge-balanced incorporation (Okumura & Kitano, 1986; Pastero & Aquilano, 2008). This mechanism explains its effective retention despite limited structural substitution.

Copper exhibited low and variable removal (70–85%), together with marked ureolysis inhibition (pH  $\approx$  6.1–6.3; [NH<sub>4</sub><sup>+</sup>]  $\approx$  1,200 ppm) and an order-of-magnitude lower carbonate yield ( $\sim$ 0.4 g) compared to Li and Zn. The small amount of blue–green precipitate formed a strongly adherent film on the filter, preventing bulk XRD/SEM characterization and suggesting nanocrystalline or amorphous Cu hydroxide/carbonate coatings rather than well-developed calcite. Similar behaviour has been reported in abiotic Cu–calcite systems, where Cu<sup>2+</sup> first adsorbs as inner-sphere, Jahn–Teller–distorted complexes at carbonate surface sites (Elzinga & Reeder, 2002; Lee et al., 2005)

and, at higher loadings, promotes the formation of basic Cu salts such as  $\text{Cu(OH)}_2$  or malachite-like  $\text{Cu}_2(\text{OH})_2\text{CO}_3$  that overgrow the carbonate surface (Papadopoulos & Rowell, 1988; Zhizhaev & Merkulova, 2014). Experimental studies further show that  $\text{Cu}^{2+}$  suppresses  $\text{CaCO}_3$  nucleation and growth by forming hydroxo- and carbonate-bearing solution complexes that block active growth sites, delaying precipitation and yielding defective or poorly ordered carbonate (Parsiegla & Katz, 2000; Caulfield et al., 2023). Taken together, these observations support a retention mechanism dominated by surface adsorption and Cu-rich amorphous or nanocrystalline coatings on biomass and nascent carbonates, rather than significant substitution of  $\text{Cu}^{2+}$  for  $\text{Ca}^{2+}$  within the calcite lattice.

Arsenic displayed the weakest overall retention (60–75%), coinciding with strong ureolysis inhibition (final pH < 7;  $[NH_4^+] \approx 1,200$ –1,400 ppm) and very low recovered solid mass, which prevented mineralogical or XRD characterisation. Under these near-neutral and reducing conditions, arsenite species are expected to dominate and interact only weakly with calcite, leading primarily to outer-sphere adsorption and/or poorly crystalline Ca–arsenite surface coatings, consistent with observations from coprecipitation and in situ AFM studies (Fernández-Martínez et al., 2006; Renard et al., 2015). Thus, the limited retention observed here is consistent with inhibited carbonate nucleation and an adsorption-dominated mechanism rather than significant structural incorporation.

Collectively, Li, Cu, and As delineate the chemical endmember of EICP immobilisation, where adsorption and redox processes dominate over lattice control. Their sequestration depends less on lattice compatibility than on surface chemistry, redox behaviour, and precipitation dynamics, marking the transition from structurally governed incorporation to adsorption-controlled immobilisation in enzyme-driven carbonate systems.

## 4.2. Organic modulation and analytical constraints

Organic constituents in the crude urease extract, especially carboxylic, phenolic, and phosphate-bearing groups, can interact with Ca<sup>2+</sup> via chelation and surface binding (Addadi & Weiner, 1985). These moieties may also stabilise early ion-association clusters or amorphous precursors that influence the initial nucleation pathway (Gower, 2008; Gebauer et al., 2008). Once crystallisation begins, such groups readily adsorb onto active crystal faces, inhibiting step propagation and altering growth kinetics, a behaviour well documented for organic carboxylates and polyelectrolytes (Amjad, 1999, 2006; Wada et al., 2001). Under higher organic loading, these interactions can further distort morphology or shift polymorph stability, consistent with observations in systems containing simple carboxylic acids and natural organic matter (Henderson et al., 2008; Amjad, 1999).

Phosphorylated proteins and phospholipids, in particular, can bind Ca<sup>2+</sup> or inhibit step-edge propagation on growing mineral surfaces—effects that typically intensify under high organic loading (Naka & Chujo, 2001; Gower, 2008). Such interactions are known to reduce crystal size, modify surface topography, and stabilise amorphous or

nanocrystalline calcium carbonate phases (Gebauer et al., 2008; Demichelis et al., 2011; Rodriguez-Navarro et al., 2015).

These effects are consistent with the morphologies observed in this study, particularly the irregular aggregates, core–shell ("sunflower") textures, and the reduced crystallinity detected in several high-metal treatments. The absence or broadening of XRD reflections in some samples likely reflects the presence of amorphous calcium carbonate (ACC) and the close association of carbonate precipitates with organic compounds, which hinder phase ordering and crystal growth. Similar behaviours have been reported in organic-rich or biologically mediated carbonate systems, where carboxylate- and phosphate-bearing macromolecules stabilise prenucleation clusters and ACC phases, delay nucleation, and promote heterogeneous growth (Addadi & Weiner, 1985; Naka & Chujo, 2001; De Yoreo, 2003; Gebauer et al., 2008; Gower, 2008; Rodriguez-Navarro et al., 2015). Such organic modulation of carbonate crystallisation is therefore consistent with both the morphological diversity and the attenuated crystallinity observed in the EICP precipitates from this study.

At the analytical level, the close association between organic matter and carbonate precipitates limits the capacity of standard characterisation techniques to resolve metal coordination environments, as SEM–EDS and FTIR cannot distinguish between lattice incorporation, surface adsorption, or amorphous binding (Reeder, 1996; Elzinga & Reeder, 2002). Achieving higher structural resolution requires advanced spectroscopic and synchrotron-based techniques such as EXAFS, ssNMR, or microdiffraction, which can directly characterise coordination environments and partitioning between organic and inorganic fractions (Blue et al., 2013).

Overall, the interaction between organic constituents and mineral formation provides a mechanistic explanation for the morphological and crystallographic variability observed across treatments. This interplay should be explicitly considered when comparing the apparent immobilisation efficiency of different metals in EICP systems.

## 4.3. Comparative performance of EICP immobilisation

When benchmarked against previous aqueous EICP studies summarised in Table 1, the present results establish a broader and more internally consistent framework for assessing metal immobilisation under enzyme-induced carbonate precipitation. Earlier studies have largely focused on a narrow subset of divalent metals, typically Pb, Cd, Zn, Ni or Cu, often examined under differing experimental conditions, urease sources and degrees of purification. By contrast, the present work evaluates nine metals simultaneously under identical aqueous conditions, including Cr, Co, Li and As, which to our knowledge have not been previously tested within the EICP context. This unified design enables direct comparison of enzymatic response, precipitation kinetics and mineralogical outcomes across a compositional spectrum spanning both structurally compatible and chemically controlled elements.

For the lattice-compatible metals (Pb, Cd, Zn, Ni and Co), the removal efficiencies obtained here (93–99 %) fall within or only slightly below the ranges reported by Wang et al. (2022, 2023), Li et al. (2022), Chen et al. (2024), Bian et al. (2024) and Xu et al. (2025), despite the lower nominal activity of the crude extract used. The agreement in both performance and mineralogy, dominance of calcite, consistent {104} displacements and minor secondary carbonates, demonstrates that high urease activity is not essential to achieve near-complete immobilisation, provided carbonate supersaturation and lattice compatibility are maintained. These observations indicate that the efficiency of metal capture in EICP is sustained even when urease activity is modest, suggesting that mineralogical processes such as coprecipitation and substitutional incorporation exert greater influence than the rate of enzymatic hydrolysis.

The chemically constrained group (Cr, Cu and As) diverges more distinctly from previous EICP reports. Chromium retained comparable overall efficiency (>85 %) to carbonate systems reported by Fang et al. (2022) yet produced finer and less ordered precipitates due to ureolysis inhibition and hydrolysis-driven nucleation. Copper and arsenic exhibited markedly lower retention (70–85 % and 60–75 %, respectively) than those observed by Xu et al. (2025) and Zeng et al. (2025), whose higher urease activities supported the formation of malachite, posnjakite or mixed basic carbonates. Here, the reduced precipitate mass and absence of resolvable crystalline phases confirm that enzyme inhibition and strong aqueous complexation limit mineralisation under more realistic biochemical conditions.

Lithium defines an intermediate behaviour not previously documented in EICP literature. Its retention (89–92 %) under fully sustained ureolysis parallels that of structurally compatible metals and provides the first experimental evidence for Li incorporation through sectoral entrapment or epitaxial coincidence in enzyme-mediated carbonates. This finding expands the known compositional range of EICP and bridges the structural–chemical divide between the classical divalent metals and those governed by adsorption or redox control.

Crude-extract EICP replicates the crystallographic and mechanistic behaviour of purified-enzyme systems under conditions representative of natural ureolysis. The resulting nine-metal dataset establishes the current compositional range of EICP and delineates the transition from substitutional incorporation to adsorption- or redox-dominated immobilisation.

# 5. Conclusions

This study demonstrates that crude soybean urease extract can drive broadspectrum removal of ecotoxic metals through enzyme-induced carbonate precipitation (EICP), achieving efficiencies comparable to or greater than systems using purified urease. Mineralogical and morphological evidence reveals dual immobilisation pathways: direct incorporation of metals into calcite lattices and modulation of mineral growth by organic biomolecules present in the crude extract. The distinctive sunflowerlike morphologies observed across treatments highlight how plant-derived organics not only catalyse ureolysis but also guide crystal formation and texture.

Across nine tested elements (As, Cd, Co, Cr, Cu, Li, Ni, Pb, and Zn), calcite consistently emerged as the dominant phase, supplemented by element-specific carbonates where thermodynamically favoured—such as cerussite (PbCO<sub>3</sub>) and otavite (CdCO<sub>3</sub>). Average removal efficiencies followed a clear sequence:

Pb > Co 
$$\approx$$
 Ni > Cd  $\approx$  Cr  $\approx$  Zn > Li > Cu  $\geq$  As

Lead achieved nearly complete removal (>99%), while Co and Ni reached 95–98%, and Cd 93-99%, forming stable carbonate solids. Cr, and Zn displayed slightly lower yet substantial efficiencies ( $\approx$ 89–95%), with outcomes more sensitive to kinetic conditions. Li, Cu, and As exhibited the lowest performance ( $\approx$ 70–92%), following alternative immobilisation pathways dominated by adsorption, amorphous carbonates, or redox effects. Notably, Cu<sup>2+</sup> and As(III) exerted strong inhibitory effects on urease activity, reducing pH and ammonium generation, while Cr showed the largest XRD {104} reflection shifts, indicative of structural distortion.

From a process perspective, this work shows that low-energy extraction, single-step clarification, and minimal reagent use can deliver strong remediation outcomes with a substantially lower chemical and energy footprint. The adaptive optimisation workflow used for crude urease extraction achieved a 54.4% reduction in total  $CO_2$ e emissions compared with conventional preparation methods, reinforcing the process's alignment with circular-economy and low-carbon engineering principles.

Although analytical-grade  $CaCl_2$  and urea were used for consistency, both could be replaced with waste-derived reagents (e.g., eggshell calcium and urine urea), aligning the process with circular-economy and greenhouse-gas reduction principles. Managing ammonium remains a critical design consideration, with feasible recovery or polishing options including struvite precipitation, zeolite ion exchange, or air stripping coupled with acid scrubbing.

Overall, crude-extract EICP represents a scalable and low-impact route for the immobilisation of toxic metals and concurrent carbon sequestration. Future research should focus on (1) testing mixed-metal systems to capture competitive and synergistic interactions, (2) resolving metal speciation and coordination at the molecular scale using EXAFS and ssNMR, and (3) integrating EICP within waste-to-reagent cycles and continuous reactor systems. Together, these directions will strengthen the foundation for field-scale deployment of this sustainable biogeotechnical technology.

#### References

Abdel-Gawwad, H. A., Hussein, Hala. S., & Mohammed, M. S. (2020). Bio-removal of Pb, Cu, and Ni from solutions as nano-carbonates using a plant-derived urease enzyme—urea mixture. *Environmental Science and Pollution Research*, *27*(24), 30741–30754. https://doi.org/10.1007/s11356-020-09359-y

Achal, V., & Pan, X. (2014). Influence of Calcium Sources on Microbially Induced Calcium Carbonate Precipitation by Bacillus sp. CR2. *Applied Biochemistry and Biotechnology*, 173(1), 307–317. https://doi.org/10.1007/s12010-014-0842-1

Addadi, L., & Weiner, S. (1985). Interactions between acidic proteins and crystals: stereochemical requirements in biomineralization. *Proceedings of the National Academy of Sciences*, 82(12), 4110–4114. https://doi.org/10.1073/pnas.82.12.4110

Ahenkorah, I., Rahman, M. M., Karim, M. R., Beecham, S., & Saint, C. (2021). A Review of Enzyme Induced Carbonate Precipitation (EICP): The Role of Enzyme Kinetics. In *Sustainable Chemistry* (Vol. 2, Issue 1, pp. 92–114). Multidisciplinary Digital Publishing Institute (MDPI). <a href="https://doi.org/10.3390/suschem2010007">https://doi.org/10.3390/suschem2010007</a>

Amjad, Z. (1999). Precipitation of calcium carbonate in aqueous systems; the influence of natural and synthetic polyelectrolytes. *Tenside Surfactants Detergents*, *36*(3), 162–167. https://doi.org/10.1515/tsd-1999-360305

Amjad, Z. (2006). Influence of natural and synthetic additives on calcium carbonate precipitation and crystal morphology. *Tenside Surfactants & Detergents*, 43(4), 184-191. https://doi.org/10.3139/113.100306

Andersson, M. P., Sakuma, H., & Stipp, S. L. S. (2014). Strontium, Nickel, Cadmium, and Lead Substitution into Calcite, Studied by Density Functional Theory. *Langmuir*, *30*(21), 6129–6133. https://doi.org/10.1021/la500832u

Baffoe, E., & Ghahremaninezhad, A. (2022). The effect of biomolecules on enzyme-induced calcium carbonate precipitation in cementitious materials. *Construction and Building Materials*, 345. https://doi.org/10.1016/j.conbuildmat.2022.128323

Bian, Y., Chen, Y., Zhan, L., Ke, H., Gao, Y., Wang, Q., & Qi, G. (2024). An Enzyme-Induced Carbonate Precipitation Method for Zn2+, Ni2+, and Cr(VI) Remediation: An Experimental and Simulation Study. *Applied Sciences (Switzerland)*, *14*(15). https://doi.org/10.3390/app14156559

Callagon, E., Fenter, P., Nagy, K. L., & Sturchio, N. C. (2014). Incorporation of Pb at the Calcite (104)–Water Interface. *Environmental Science & Technology*, 48(16), 9263–9269. https://doi.org/10.1021/es5014888

Callagon, E. B. R., Lee, S. S., Eng, P. J., Laanait, N., Sturchio, N. C., Nagy, K. L., & Fenter, P. (2017). Heteroepitaxial growth of cadmium carbonate at dolomite and calcite

surfaces: Mechanisms and rates. *Geochimica et Cosmochimica Acta*, 205, 360–380. https://doi.org/10.1016/j.gca.2016.12.007

Caulfield, B., Roberts, M., & Prigiobbe, V. (2023). Studying the effect of nickel, copper, and zinc on the precipitation kinetics and the composition of Ca-carbonates for the integrated process of CO<sub>2</sub> mineralization and brine mining. *Chemical Engineering Journal*, 476, 146220. https://doi.org/10.1016/j.cej.2023.146220

Chen, Y., Wang, Q., Bian, Y., Zhan, L., Gao, Y., Guo, H., Wang, Y., & Gao, Y. (2024). Effects of enzyme-induced carbonate precipitation (EICP) with different urease sources on the zinc remediation. *Journal of Hazardous Materials*, *480*. https://doi.org/10.1016/j.jhazmat.2024.136321

Chen, Y., Bian, Y., Zhan, L., Wang, Y., Gao, Y., & Wang, L. (2025). Effects of multi-source plant-derived urease enzyme on the morphology, growth, size, and distribution behavior of calcium carbonate through enzyme-induced carbonate precipitation method: a microfluidic chip experiment. *Acta Geotechnica*. <a href="https://doi.org/10.1007/s11440-025-02586-y">https://doi.org/10.1007/s11440-025-02586-y</a>

Davis, J. A., Fuller, C. C., & Cook, A. D. (1987). A model for trace metal sorption processes at the calcite surface: Adsorption of Cd\*+ and subsequent solid solution formation. *Geochimica et Cosmochimica Acta*, *51*.

Demichelis, R., Raiteri, P., Gale, J. D., Quigley, D., & Gebauer, D. (2011). Stable prenucleation mineral clusters are liquid-like ionic polymers. *Nature Communications*, 2(1), 590. https://doi.org/10.1038/ncomms1604

de Yoreo, J. J. (2003). Principles of Crystal Nucleation and Growth. *Reviews in Mineralogy and Geochemistry*, *54*(1), 57–93. https://doi.org/10.2113/0540057

Dickinson, H., MacDonald, J., & Toney, J. L. (2025). Enzyme-mediated multiphase precipitation: An innovative strategy for ecotoxic metal immobilization in aqueous systems. *Journal of Environmental Chemical Engineering*, *13*(5), 119087. https://doi.org/10.1016/j.jece.2025.119087

Doebelin, N., & Kleeberg, R. (2015). *Profex*: a graphical user interface for the Rietveld refinement program *BGMN*. *Journal of Applied Crystallography*, *48*(5), 1573–1580. https://doi.org/10.1107/S1600576715014685

Elzinga, E. J., & Reeder, R. J. (2002). X-ray absorption spectroscopy study of Cu2+ and Zn2+ adsorption complexes at the calcite surface. *Geochimica et Cosmochimica Acta*, 66(22), 3943–3954. https://doi.org/10.1016/S0016-7037(02)00971-7

Elzinga, E. J., Rouff, A. A., & Reeder, R. J. (2006). The long-term fate of Cu2+, Zn2+, and Pb2+ adsorption complexes at the calcite surface: An X-ray absorption spectroscopy study. *Geochimica et Cosmochimica Acta*, *70*(11), 2715–2725. https://doi.org/10.1016/j.gca.2006.02.026

Fang, Z., Liu, W., Yao, T., Zhou, G., Wei, S., & Qin, L. (2022). Experimental study of chromium (III) coprecipitation with calcium carbonate. *Geochimica et Cosmochimica Acta*, 322, 94–108. https://doi.org/10.1016/j.gca.2022.01.019

Fernández-Martínez, A., Román-Ross, G., Cuello, G. J., Turrillas, X., Charlet, L., Johnson, M. R., & Bardelli, F. (2006). Arsenic uptake by gypsum and calcite: Modelling and probing by neutron and X-ray scattering. *Physica B: Condensed Matter*, *385*–*386*, 935–937. https://doi.org/10.1016/j.physb.2006.05.276

Freij, S. J., Putnis, A., & Astilleros, J. M. (2004). Nanoscale observations of the effect of cobalt on calcite growth and dissolution. *Journal of Crystal Growth*, *267*(1–2), 288–300. https://doi.org/10.1016/j.jcrysgro.2004.03.044

García-Sánchez, A., & Álvarez-Ayuso, E. (2002). Sorption of Zn, Cd and Cr on calcite. Application to purification of industrial wastewaters. *Minerals Engineering*, *15*(7), 539–547. https://doi.org/10.1016/S0892-6875(02)00072-9

Gebauer, D., Völkel, A., & Cölfen, H. (2008). Stable Prenucleation Calcium Carbonate Clusters. *Science*, *322*(5909), 1819–1822. https://doi.org/10.1126/science.1164271

Gilmour, K. A., Ghimire, P. S., Wright, J., Haystead, J., Dade-Robertson, M., Zhang, M., & James, P. (2024). Microbially induced calcium carbonate precipitation through CO2 sequestration via an engineered Bacillus subtilis. *Microbial Cell Factories*, *23*(1), 168. https://doi.org/10.1186/s12934-024-02437-7

González-López, J., Ruiz-Hernández, S. E., Fernández-González, Á., Jiménez, A., de Leeuw, N. H., & Grau-Crespo, R. (2014). Cobalt incorporation in calcite: Thermochemistry of (Ca,Co)CO 3 solid solutions from density functional theory simulations. *Geochimica et Cosmochimica Acta*, *142*, 205–216. https://doi.org/10.1016/j.gca.2014.07.026

Gower, L. B. (2008). Biomimetic model systems for investigating the amorphous precursor pathway and its role in biomineralization. *Chemical Reviews*, *108*(11), 4551–4627. https://doi.org/10.1021/cr800443h

Hemayati, M., Aghaei, H., Daman Shokouh, A., Nikooee, E., Niazi, A., & Khodadadi Tirkolaei, H. (2024). A pore-scale study of fracture sealing through enzymatically-induced carbonate precipitation (EICP) method demonstrates its potential for CO2 storage management. *Scientific Reports*, *14*(1), 17832. <a href="https://doi.org/10.1038/s41598-024-68720-0">https://doi.org/10.1038/s41598-024-68720-0</a>

Henderson, G. E., Murray, B. J., & McGrath, K. M. (2008). Controlled variation of calcite morphology using simple carboxylic acids. *Journal of Crystal Growth*, *310*(18), 4190–4198. https://doi.org/10.1016/j.jcrysgro.2008.07.002

Kim, J. J., Lee, S. S., Fenter, P., Myneni, S. C. B., Nikitin, V., & Peters, C. A. (2023). Carbonate Coprecipitation for Cd and Zn Treatment and Evaluation of Heavy Metal

Stability Under Acidic Conditions. *Environmental Science & Technology*, *57*(8), 3104–3113. https://doi.org/10.1021/acs.est.2c07678

Lakshtanov, L. Z., & Stipp, S. L. S. (2007). Experimental study of nickel(II) interaction with calcite: Adsorption and coprecipitation. *Geochimica et Cosmochimica Acta*, *71*(15), 3686–3697. <a href="https://doi.org/10.1016/j.gca.2007.04.006">https://doi.org/10.1016/j.gca.2007.04.006</a>

Lee, Y. J., Elzinga, E. J., & Reeder, R. J. (2005). Cu(II) adsorption at the calcite–water interface in the presence of natural organic matter: Kinetic studies and molecular-scale characterization. *Geochimica et Cosmochimica Acta*, 69(1), 49–61. https://doi.org/10.1016/j.gca.2004.06.015

Lee, H. H. (2025). Adsorption characteristics of cadmium onto calcite and its agricultural environmental relevance. *Heliyon*, *11*(1). https://doi.org/10.1016/j.heliyon.2024.e40241

Li, W., Zhang, Y., & Achal, V. (2022). Mechanisms of cadmium retention on enzyme-induced carbonate precipitation (EICP) of Ca/Mg: Nucleation, chemisorption, and co-precipitation. *Journal of Environmental Chemical Engineering*, *10*(3). https://doi.org/10.1016/j.jece.2022.107507

Ma, C., Xu, F., Zhu, Z., Yang, H., Nong, P., Kang, Z., Tang, S., Zhang, L., & Zhu, Y. (2022). Dissolution and Solubility of the Calcite–Otavite Solid Solutions [(Ca1-x Cdx)CO3] at 2° C. *Minerals*, *12*(6). https://doi.org/10.3390/min12060756

McBride, M. B. (1980). Chemisorption of Cd2+ on Calcite Surfaces. *Soil Science Society of America Journal*, 44(1), 26–28.

https://doi.org/10.2136/sssaj1980.03615995004400010006x

Morse, J. W., Arvidson, R. S., & Lüttge, A. (2007). Calcium Carbonate Formation and Dissolution. *Chemical Reviews*, 107(2), 342–381. https://doi.org/10.1021/cr050358j

Naka, K., & Chujo, Y. (2001). Control of Crystal Nucleation and Growth of Calcium Carbonate by Synthetic Substrates. *Chemistry of Materials*, *13*(10), 3245–3259. https://doi.org/10.1021/cm011035g

Okumura, M., & Kitano, Y. (1986). Coprecipitation of alkali metal ions with calcium carbonate. *Geochimica et Cosmochimica Acta*, *50*(1), 49–58. https://doi.org/10.1016/0016-7037(86)90047-5

Orme CA, Noy A, Wierzbicki A, McBride MT, Grantham M, Teng HH, Dove PM, DeYoreo JJ. Formation of chiral morphologies through selective binding of amino acids to calcite surface steps. Nature. 2001 Jun 14;411(6839):775-9. doi: 10.1038/35081034. PMID: 11459051

Papadopoulos, P., & Rowell, D. L. (1988). The reactions of cadmium with calcium carbonate surfaces. *Journal of Soil Science*, *39*(1), 23–36. https://doi.org/10.1111/j.1365-2389.1988.tb01191.x

Pastero, L., Costa, E., Bruno, M., Rubbo, M., Sgualdino, G., & Aquilano, D. (2004). Morphology of Calcite (CaCO <sub>3</sub>) Crystals Growing from Aqueous Solutions in the Presence of Li <sup>†</sup> Ions. Surface Behavior of the {0001} Form. *Crystal Growth & Design*, *4*(3), 485–490. https://doi.org/10.1021/cg034217r

Parsiegla, K. I., & L. Katz, J. (2000). Calcite growth inhibition by copper(II). *Journal of Crystal Growth*, *213*(3–4), 368–380. https://doi.org/10.1016/S0022-0248(00)00306-7

Putnis, A., & Putnis, C. v. (2007). The mechanism of reequilibration of solids in the presence of a fluid phase. *Journal of Solid State Chemistry*, *180*(5), 1783–1786. https://doi.org/10.1016/j.jssc.2007.03.023

Rai, D., Moore, D. A., Hess, N. J., Rosso, K. M., Rao, L., & Heald, S. M. (2007). Chromium(III) hydroxide solubility in the aqueous K+-H+-OH--CO2-HCO 3--CO 32--H2O system: A thermodynamic model. *Journal of Solution Chemistry*, *36*(10), 1261–1285. https://doi.org/10.1007/s10953-007-9179-5

Rajasekar, A., Omoregie, A. I., & Kui, K. F. (2025). Urease-catalyzed microbial and enzymatic carbonate precipitation for eco-friendly heavy metal remediation. In *Letters in Applied Microbiology* (Vol. 78, Issue 2). Oxford University Press. https://doi.org/10.1093/lambio/ovaf022

Reeder, R. J. (1996). Interaction of divalent cobalt, zinc, cadmium, and barium with the calcite surface during layer growth. In *Pergamon Geochimica et Cosmochimica Acta* (Vol. 60, Issue 9).

Reeder, R. J., Lamble, G. M., & Northrup, P. A. (1999). XAFS study of the coordination and local relaxation around Co 2+, Zn 2+, Pb 2+, and Ba 2+ trace elements in calcite BACKGROUND AND SCOPE. In *American Mineralogist* (Vol. 84).

Renard, F., Putnis, C. v., Montes-Hernandez, G., Ruiz-Agudo, E., Hovelmann, J., & Sarret, G. (2015). Interactions of arsenic with calcite surfaces revealed by in situ nanoscale imaging. *Geochimica et Cosmochimica Acta*, *159*, 61–79. https://doi.org/10.1016/j.gca.2015.03.025

Riechers, S. L., Ilton, E. S., Qafoku, O., Du, Y., & Kerisit, S. N. (2022). Cobalt hydroxide–cobalt carbonate competitive growth on carbonate surfaces. *Chemical Geology*, 605. https://doi.org/10.1016/j.chemgeo.2022.120951

Rodriguez-Navarro, C., Kudłacz, K., Cizer, Ö., & Ruiz-Agudo, E. (2015). Formation of amorphous calcium carbonate and its transformation into mesostructured calcite. *CrystEngComm*, *17*(1), 58–72. https://doi.org/10.1039/C4CE01562B

Rouff, A. A., Reeder, R. J., & Fisher, N. S. (2002). Pb (II) Sorption with Calcite: A Radiotracer Study. In *Aquatic Geochemistry* (Vol. 8).

Saif, A., Cuccurullo, A., Gallipoli, D., Perlot, C., & Bruno, A. W. (2022). Advances in Enzyme Induced Carbonate Precipitation and Application to Soil Improvement: A Review. In *Materials* (Vol. 15, Issue 3). MDPI. <a href="https://doi.org/10.3390/ma15030950">https://doi.org/10.3390/ma15030950</a>

Sikirić, M. D., & Füredi-Milhofer, H. (2006). The influence of surface active molecules on the crystallization of biominerals in solution. *Advances in Colloid and Interface Science*, 128–130, 135–158. https://doi.org/10.1016/j.cis.2006.11.022

Shu, S., Yan, B., Ge, B., Li, S., & Meng, H. (2022). Factors Affecting Soybean Crude Urease Extraction and Biocementation via Enzyme-Induced Carbonate Precipitation (EICP) for Soil Improvement. *Energies*, *15*(15). https://doi.org/10.3390/en15155566

Stipp, S. L., Hochella, M. F., Park&~, G. A., & Leckie', J. 0. (1992). Cd\*+ uptake by caicite, solid-state diffusion, and the formation of solid-solution: Interface processes observed with near-surface sensitive techniques (XI'S, LEED, and AES). In *Geochimica ef Cosmochimica Acfa* (Vol. 56).

Sturchio, N. C., Chiarello, R. P., Cheng, L., Lyman, P. F., Bedzyk, M. J., Qian, Y., You, H., Yee, D., Geissbuhler, P., Sorensen, L. B., Liang, Y., & Baer, D. R. (1997). Lead adsorption at the calcite-water interface: Synchrotron X-ray standing wave and X-ray reflectivity studies. *Geochimica et Cosmochimica Acta*, *61*(2), 251–263. https://doi.org/10.1016/S0016-7037(96)00326-2

United Nations Environment Programme (UNEP) (2021) Food Waste Index Report 2021. Nairobi. 2021 United Nations Environment Programme.

https://www.unep.org/resources/report/unep-food-waste-index-report-2021

Wada, N., Kanamura, K., & Umegaki, T. (2001). Effects of carboxylic acids on the crystallization of calcium carbonate. *Journal of Colloid and Interface Science*, 233(1), 65–72. https://doi.org/10.1006/jcis.2000.7215

Wang, L., Cheng, W.-C., & Xue, Z.-F. (2022a). The Effect of Calcium Source on Pb and Cu Remediation Using Enzyme-Induced Carbonate Precipitation. *Frontiers in Bioengineering and Biotechnology*, 10. https://doi.org/10.3389/fbioe.2022.849631

Wang, L., Cheng, W. C., Xue, Z. F., & Hu, W. (2022b). Effects of the Urease Concentration and Calcium Source on Enzyme-Induced Carbonate Precipitation for Lead Remediation. *Frontiers in Chemistry*, 10. https://doi.org/10.3389/fchem.2022.892090

Wang, L., Cheng, W. C., Xue, Z. F., Zhang, B., & Lv, X. J. (2023). Immobilizing of lead and copper using chitosan-assisted enzyme-induced carbonate precipitation. *Environmental Pollution*, 319. https://doi.org/10.1016/j.envpol.2022.120947

Weiner, S., & Addadi, L. (2011). Crystallization Pathways in Biomineralization. *Annual Review of Materials Research*, *41*(1), 21–40. <a href="https://doi.org/10.1146/annurev-matsci-062910-095803">https://doi.org/10.1146/annurev-matsci-062910-095803</a>

Wu, Q., Huang, Y., Irga, P., Kumar, P., Li, W., Wei, W., Shon, H. K., Lei, C., & Zhou, J. L. (2024). Synergistic control of urban heat island and urban pollution island effects using green infrastructure. In *Journal of Environmental Management* (Vol. 370). Academic Press. https://doi.org/10.1016/j.jenvman.2024.122985

Xu, M., Ilton, E. S., Engelhard, M. H., Qafoku, O., Felmy, A. R., Rosso, K. M., & Kerisit, S. (2015). Heterogeneous growth of cadmium and cobalt carbonate phases at the calcite {1014} surface. *Chemical Geology, 397*, 24–36.

https://doi.org/10.1016/j.chemgeo.2015.01.003

Xu, W., Zheng, J., Cui, M., & Lai, H. (2025). Enzyme-Induced Carbonate Precipitation for the Stabilization of Heavy Metal-Contaminated Landfill Soils: A Sustainable Approach to Resource Recovery and Environmental Remediation. *Sustainability (Switzerland)*, 17(10). https://doi.org/10.3390/su17104630

Zeng, H., Jin, B., Xu, S., Han, L., Wang, J., Jia, H., Dapaah, M. F., & Cheng, L. (2025). Removal of copper, lead and cadmium from water through enzyme-induced carbonate precipitation by soybean urease. *Environmental Research*, *277*. https://doi.org/10.1016/j.envres.2025.121610

Zhizhaev, A. M., & Merkulova, E. N. (2014). Interaction of copper(II) and zinc(II) in coprecipitation from sulfate solutions with natural calcium carbonate. *Russian Journal of Applied Chemistry*, 87(1), 16–22. https://doi.org/10.1134/S1070427214010029